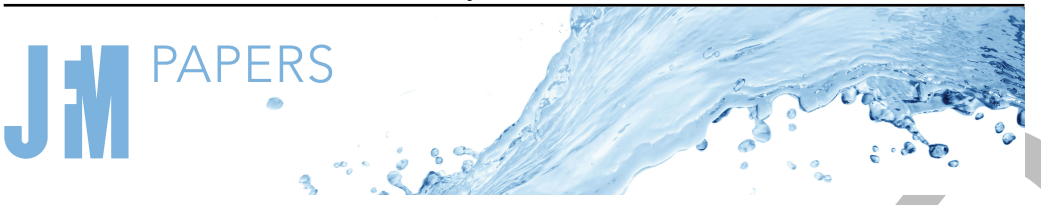
J. Fluid Mech. (2026), *vol.* 1036, A34, doi:10.1017/jfm.2025.10905



RETRACTED - Instabilities in separation and reattachment induced by a hypersonic shock-wave/boundary-layer interaction

Jonathan Davami[1,2], Anton Scholten[3], Pedro Paredes[2], Nolan Little[4], Lian Duan[4] and Thomas Juliano[1]

[1]Department of Aerospace and Mechanical Engineering, University of Notre Dame, Notre Dame, IN 46556, USA

[2]NASA Langley Research Center, Hampton, VA 23681 USA

[3]National Institute of Aerospace, Hampton, VA 23666, USA

[4]Department of Mechanical and Aerospace Engineering, The Ohio State University, Columbus, OH 43210, USA

Corresponding author: Thomas Juliano, tjuliano@nd.edu

(Received 8 April 2025 UTC; revised 17 October 2025 UTC; accepted 24 October 2025 UTC)

Mean flow and instability measurements of a nominally axisymmetric, transitional separation bubble arising from a flare-induced shock-wave/boundary-layer interaction were conducted on a cone–flare geometry in hypersonic flow. Simultaneous infrared thermography and high-speed, high-resolution background-oriented schlieren measurements provided a global, time-resolved characterisation of both the mean and unsteady flow. Experiments were performed in the AFOSR–Notre Dame Large Mach-6 Quiet Tunnel under conventional noise at free-stream unit Reynolds numbers ranging from 5.8×10^6 to 12.3×10^6 m^{-1}. The model comprised a 7° half-angle circular cone, a 20° half-angle flare and three nose radii. Complementary laminar and turbulent base flows, convective and global stability analyses (GSAs) and direct numerical simulations (DNSs) were carried out at the experimental conditions. With inflow forcing of disturbances, the DNS reproduces the experimentally observed flare-heating trends. While the flow is convectively unstable, global instability arises specifically from stationary and oscillatory three-dimensional disturbances localised within the recirculation bubble. Thermal streaks observed in global heating measurements provide experimental evidence of these instabilities, which is further corroborated by the onset of three-dimensionality in DNS. Quantitative agreement of streak wavelengths and their spatial prevalence across experiments, GSAs and DNSs confirms that the recirculation bubble's global instability

© National Aeronautics and Space Administration (NASA) and the Author(s), 2026. To the extent this is a work of the US Government, it is not subject to copyright protection within the United States. Published by Cambridge University Press. This is an Open Access article, distributed under the terms of the Creative Commons Attribution licence (https://creativecommons.org/licenses/by/4.0/), which permits unrestricted re-use, distribution and reproduction, provided the original article is properly cited.

RETRACTED

https://doi.org/10.1017/jfm.2025.10905

is the primary driver of the reattachment streaks in this flow, providing the first direct experimental evidence of this mechanism.

Key words: boundary layer separation, boundary layer stability, hypersonic flow

1. Introduction

Limited understanding of laminar-to-turbulent transition constrains hypersonic vehicle design since boundary-layer transition leads to extreme thermo-mechanical surface loads (Schneider 2004; Horvath, Berry & Merski 2004; Lee & Chen 2019). While turbulent boundary layers produce higher surface heating than laminar ones, transitional heating can significantly exceed turbulent heating rates (Schneider 2001; Stanfield, Kimmel & Adamczak 2015; Juliano, Jewell & Kimmel 2021). Due to the challenges in predicting the breakdown of instability mechanisms (Paredes, Choudhari & Li 2020; Yang *et al.* 2022; Sombaert *et al.* 2025*a*; Chynoweth, Lay & Jewell 2025), the presence, location and magnitude of this overshoot remains uncertain (Franko & Lele 2013; De Tullio *et al.* 2013; Hader & Fasel 2018, 2020; Paredes *et al.* 2020; Hill *et al.* 2022).

Although most hypersonic transition research has focused on attached boundary layers (Fedorov 2011; Lee & Chen 2019; Wheaton *et al.* 2021; Sombaert *et al.* 2025*b*), the stability of separated flows is also a critical concern. Abrupt changes of flow direction, e.g. at control surfaces or intakes, can result in shock waves whose strong adverse pressure gradients can induce boundary-layer separation, resulting in shock-wave/boundary-layer interactions (SWBLIs) and the formation of recirculation bubbles (Babinsky & Harvey 2011). The multi-scale dynamics of a separation region affects transition, while transition also impacts the bubble, creating a complex, interdependent problem. Understanding the mechanisms of transition in SWBLIs is essential for predicting, delaying or controlling the associated adverse effects (Watts 1968; Holden 1986; Iliff & Shafer 1993).

A SWBLI is strongly influenced by the state of the boundary layer – whether laminar, transitional, or turbulent – incoming to the interaction. Laminar boundary layers frequently result in large separated regions characterised by a low-frequency, large-scale dynamics (Grasso & Marini 1996; Clemens & Dolling 2014; Running & Juliano 2021). Turbulent boundary layers, with their higher momentum near the wall, are less prone to separation and thus often engender small or absent separated regions (Green 1970; Holden 1972; Running *et al.* 2019). Prior work has primarily focused on fully laminar or turbulent SWBLIs; however, transitional interactions, which are commonly encountered in hypersonic flight, can produce heating levels exceeding fully turbulent cases (Berry *et al.* 2001; Weihs, Longo & Turner 2008; Bur & Chanetz 2009; Davami *et al.* 2025*c*). Transitional SWBLIs often involve concurrent instability mechanisms with potential for complex mode coupling, presenting a challenging problem for both simulation and measurement (Currao *et al.* 2020; Threadgill *et al.* 2021, 2024; Benitez *et al.* 2025; Caillaud *et al.* 2025; Mauriello *et al.* 2025; Prasad, Sarath & Unnikrishnan 2025; Davami *et al.* 2025*d*). Despite their prevalence, comprehensive coupled experimental (ground and flight) and computational studies remain exceptionally scarce (Willems *et al.* 2024; Davami *et al.* 2025*c*), underscoring the need for further research in this area.

This work examines a cone–flare model at zero angle of attack, featuring a nominally axisymmetric SWBLI. For this geometry, the second-mode instability is expected to determine the boundary-layer state approaching the compression corner (Mack 1984). Its growth depends on the free-stream conditions, nose radius, surface roughness,

RETRACTED

https://doi.org/10.1017/jfm.2025.10905

wall temperature and cone angle. The strength of the SWBLI depends on the free-stream stagnation enthalpy, free-stream Mach number, wall temperature and flare angle (Babinsky & Harvey 2011; Bibin *et al.* 2016). Depending on the boundary-layer state and SWBLI strength, the boundary layer may separate, inducing a separation shock; subsequent reattachment on the flare requires a reattachment shock as the flow turns parallel to the surface. The topology of the bubble between separation and reattachment can be complex, often containing multiple separated regions and recirculation zones (Song & Hao 2023).

In addition to their sensitivity to upstream instabilities, SWBLIs exhibit instabilities that affect their downstream development (Balakumar, Zhao & Atkins 2005; Cao, Hao & Guo 2024). The SWBLI flows with laminar incoming boundary layers are prone to instabilities such as shear-layer waves (Lugrin *et al.* 2022*b*; Benitez *et al.* 2023; Davami *et al.* 2025*c*,*d*), shock-layer waves (Davami *et al.* 2024; Benitez *et al.* 2024*b*; Davami *et al.* 2025*a*,*c*), Görtler vortices (Ginoux 1971; Chuvakhov & Egorov 2017) and reattachment vortices (Gray 1967; Running *et al.* 2020; Lugrin *et al.* 2022*b*; Benitez *et al.* 2024*a*). Streamwise vortices near reattachment of separation bubbles can precipitate or accelerate transition (Theofilis, Hein & Dallmann 2000; Hildebrand *et al.* 2018; Paredes *et al.* 2022; Prasad *et al.* 2025). They induce alternating regions of upwash and downwash via counter-rotating vortex pairs, which have been shown to exhibit characteristic azimuthal wavelengths (Roghelia *et al.* 2017; Running *et al.* 2020), producing periodic variations in skin friction and heat flux that appear as streamwise heating streaks. Ginoux (1965) first documented their occurrence in a variety of separated flows – including cavities, forward-facing steps, compression ramps and hollow-cylinder flares – across a wide Mach number range of 1.5–7, and noted their presence in laminar, transitional and turbulent flows (Ginoux 1971).

Despite being discovered nearly 60 years ago, the origin of the streaks is still not entirely understood. Numerous computational and experimental studies on compression ramps suggest the streaks are caused by Görtler-like vortices (Görtler 1940; Currao *et al.* 2021; Xu, Chen & Liu 2024; Tsakagiannis *et al.* 2025*b*), triggered by upstream disturbances, which intensify due to centrifugal effects from concave streamline curvature along the separated shear layer near reattachment (Inger 1977; Comte 1999; Adams 2000; Benay *et al.* 2006). However, comparisons with Görtler instability theory remain qualitative and do not account for the dynamics of the separation bubble (Dwivedi *et al.* 2019). Furthermore, the azimuthal spacing of Görtler-like vortices is known to be Reynolds-number-independent and can be primarily influenced by the model geometry (de la Chevalerie *et al.* 1997), which contrasts with other studies that have examined the variation of streak intensity with Reynolds number (Gray 1967; Chuvakhov & Egorov 2017; Running *et al.* 2020; Lugrin *et al.* 2022*b*). More recent studies indicate that multiple mechanisms, including convective and global (absolute) instabilities, can drive the formation of reattachment streaks and promote transition to turbulence (Cao *et al.* 2021; Hao, Cao & Wen 2021; Lugrin *et al.* 2022*b*; Dwivedi, Sidharth & Jovanović 2022; Davami *et al.* 2023*b*; Scholten 2024).

Global instability of separated flows arises from the temporal amplification of stationary and oscillatory three-dimensional disturbances confined within recirculation bubbles. Global stability analysis (GSA) has been used extensively on high-speed separation bubbles to investigate unstable global modes (i.e. unstable eigenfunctions of the linearised Navier–Stokes operator) (Robinet 2007; Gómez *et al.* 2012; Paredes *et al.* 2022; Davami *et al.* 2025*c*). It examines the temporal stability of small disturbances imposed on steady two-dimensional and axisymmetric base flows with spatial variation (Sipp & Lebedev 2010; Paredes 2014). Through GSA, Robinet (2007), Paredes *et al.* (2022),

RETRACTED

https://doi.org/10.1017/jfm.2025.10905

Song & Hao (2023) have shown that two-dimensional (2-D) SWBLIs become globally unstable within the separation bubble once the interaction strength exceeds a critical threshold. Sidharth & Candler (2018) and Hildebrand *et al.* (2018) demonstrated that for globally unstable transitional SWBLIs, global unstable modes within the recirculation bubble drive the formation of streamwise streaks. Their analysis indicated that a Görtler-like centrifugal instability did not influence the upstream self-sustaining mechanism of the global instability, although both mechanisms may coexist. The global instability alone causes spanwise modulation of the flow, inducing streaks that breakdown to turbulence downstream of reattachment. Cao *et al.* (2021) also showed that nonlinear saturation of globally unstable modes could give rise to striations.

Even globally stable separated flows are highly sensitive to vortical disturbances. Dwivedi *et al.* (2019) demonstrated that non-modal amplification of small fluctuations can produce steady streaks near reattachment. Cao *et al.* (2024) showed, using resolvent and local stability analyses supported by direct numerical simulations (DNSs) with inflow forcing, that transition downstream of reattachment can proceed either via strong streak breakdown or second-mode amplification, depending on the prescribed amplitude of upstream disturbances. Both experimental (Davami *et al.* 2025*d*) and computational (Saïdi *et al.* 2025) studies show that SWBLI-induced transition is governed by coherent triadic cascades of sum- and difference-frequency interactions concentrated near reattachment. Dwivedi *et al.* (2022) revealed in simulations that these quadratic interactions give rise to reattachment streaks, which then amplify and trigger transition to turbulence.

The dominant spanwise wavelength of the streaks depends on the geometry and flow conditions. Running *et al.* (2020) was the first to experimentally quantify it on a cone–flare model in high-speed flow, using spectral analysis on global Stanton number distributions obtained from infrared (IR) thermography for flare half-angles of 34° to 43°. The dominant wavelengths increased for increasing flare angle, independent of the incoming boundary-layer state. The variation in the streaks' azimuthal amplitude was significantly lower than in compression-ramp studies (Roghelia *et al.* 2017), hinting at a fundamental difference between axisymmetric and 2-D SWBLIs. Sun *et al.* (2025) used high-fidelity computations to confirm the experimentally observed differences in streak intensity. Lugrin *et al.* (2022*b*) performed IR measurements on a hollow-cylinder flare in hypersonic flow to study the streaks, showing multiple mechanisms likely lead to their formation. Benitez *et al.* (2024*a*) conducted IR measurements on a cone-cylinder flare in conventional-noise hypersonic flow, observing that streamwise streaks became more pronounced with increased nose bluntness. This differs from the result on 2-D compression ramps, for which increased bluntness significantly reduces spanwise heating variation (Roghelia *et al.* 2017).

Most prior coupled experimental–computational studies of SWBLI have concentrated on convectively unstable flows, which lack self-sustained instabilities, but act as effective noise amplifiers by magnifying incoming disturbances (Dwivedi *et al.* 2019, 2022; Niessen *et al.* 2023; Cao *et al.* 2024; Tsakagiannis *et al.* 2025*a*). While such configurations have been useful for isolating and characterising convective amplification mechanisms, they do not capture the broader spectrum of instability dynamics that can arise in separated hypersonic flows. The present study extends this scope by investigating a regime that is both convectively and globally unstable, using high-fidelity simulations in tandem with detailed experimental measurements to identify the instabilities governing transition in a nominally axisymmetric separation bubble, and providing direct experimental validation of the stability analysis predictions. To this end, experiments were conducted on a cone–flare model in the AFOSR–Notre Dame Large Mach-6 Quiet Tunnel under conventional-noise conditions, across a range of Reynolds numbers and three nose radii at nominally zero angle of attack. Simultaneous IR thermography and high-speed,

https://doi.org/10.1017/jfm.2025.10905

RETRACTED

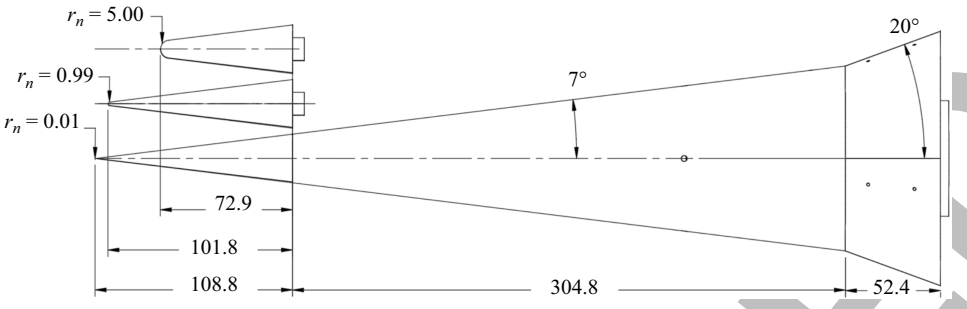


Figure 1. Illustration of the cone–flare test article (dimensions are in millimetres).

high-resolution background-oriented schlieren (BOS) measurements provided a global, time-resolved characterisation of both mean and unsteady features of the flare-induced SWBLI. High-resolution BOS yielded quantitative off-wall density and density-gradient fields, while high-speed measurements captured the separation-bubble dynamics. Infrared thermography assessed flow stability and boundary-layer state. Combining surface and off-wall measurements allowed documentation of trends in separation, reattachment and transition locations across Reynolds numbers and nose radii. Experimentally observed streaks near reattachment indicate unstable azimuthally periodic perturbations. Global stability analysis confirmed the flow is globally unstable, and comparison of experimentally measured azimuthal wavenumbers with GSA and DNS results evaluates the role of global instability in forming streamwise streaks.

2. Model, facility and test conditions

2.1. *Model*

The test article is a 7° half-angle circular cone and 20° half-angle flare (figure 1). It consists of three main components: three interchangeable nose tips, a frustum and four flare petals. The frustum and flare petals have surface-normal holes for pressure sensors. The noses were fabricated from stainless steel, with nose radii of $r_n = 0.01$, 0.99 and 5.00 mm. The flare petals and frustum were fabricated from aluminium. Due to the various nose radii tested, the cone length L is not constant and depends on the nose radius r_n. The x-coordinate is defined from the tip the respective nose used in the experiment.

2.2. *Facility*

Experiments were conducted in the Air Force Office of Scientific Research–Notre Dame Large Mach-6 Quiet Tunnel (ANDLM6QT). The ANDLM6QT has a 60 m-long driver tube and 63 cm nozzle exit diameter (Lakebrink, Borg & Kimmel 2018). Heating blankets on the driver tube permit stagnation temperatures from 435 to 590 K. A pneumatically actuated fast-acting shutter valve at the contraction exit opens to start a run, which lasts ≈ 1 s. During a test run, the variation in the free-stream unit Reynolds number is less than 10 %. The ANDLM6QT is operational with conventional-noise levels of 1.6 %–2.3 %, depending on free-stream Reynolds number, and a free-stream Mach number of 5.7 (Lawson 2025), typical for a conventional-noise tunnel (Schneider 2000, 2001; Duan *et al.* 2018).

2.3. *Test conditions*

Five free-stream unit Reynolds numbers were tested for each nose radius. Table 1 summarises the flow conditions with corresponding uncertainties. Sutherland's law was

RETRACTED

https://doi.org/10.1017/jfm.2025.10905

M_∞ (±0.04)	P_0 (kPa) (±8)	T_0 (K) (±3)	ρ_0 (kg m^{-3}) (±0.10)	P_∞ (kPa) (±0.01)	T_∞ (K) (±0.5)	ρ_∞ (kg m^{-3}) (±0.001)	U_∞ (m s^{-1}) (±7.0)	Re_∞ ($\times 10^6$ m^{-1}) (±0.1)	Re_L ($\times 10^6$) (±0.1)
5.70	490	435	3.92	0.424	58.1	0.026	870.6	5.8	2.4
5.70	642	435	5.13	0.552	57.8	0.033	870.4	7.6	3.1
5.70	706	436	5.64	0.612	58.1	0.037	871.2	8.4	3.4
5.70	841	437	6.71	0.729	58.3	0.045	872.3	10.0	4.0
5.70	1013	436	8.10	0.878	58.1	0.053	871.2	12.0	4.9

Table 1. Flow conditions.

used to compute viscosity (Sutherland 1893). The free-stream quantities were computed using isentropic relations with the measured time-varying stagnation pressure, initial stagnation temperature and measured Mach number from Hoberg & Juliano (2023).

3. Instrumentation and data reduction methodology

3.1. *PCB piezotronics pressure sensors*

Four PCB Piezotronics 132B38 pressure sensors were used to measure pressure fluctuations on the model's conical forebody, primarily for alignment with the flow (§ 4). Their measurement range is 345 kPa, sensitivity is 20.3 mV/kPa and resolution is 7 Pa. Their low-frequency limit is 11 kHz, and high-frequency response limit is 1 MHz. The conversion from measured voltage to pressure fluctuation was performed using the PCB factory calibration. The sensors were sampled at 2 MHz using a HBM Genesis 17ta data-acquisition system.

3.2. *Infrared thermography*

The model surface temperature was measured with a 14-bit InfraTech 8300 hp IR camera with a spectral range of 2.0–5.5 µm (mid-wave IR). The camera resolution is 640 × 512 pixels with a frame rate set to 355 fps. A 25 mm focal length lens was used with its factory calibration. The spatial resolution of the measurements was 0.20 mm. The overall relative uncertainty of the IR camera temperature measurement is ±0.4 %, in which the systematic uncertainty and resolution are ±1 K and 0.02 K, respectively (InfraTec 2016).

Aluminium's low surface emissivity was addressed by applying a matte-black self-adhesive film (3M^{TM} Wrap Film Series 1080) to a 180° sector of the frustum and flare for improved IR thermography (Running *et al.* 2022). The vinyl wrap footprint was evaluated using a computer-aided design sheet-metal feature, and fiducial marks (0.5 mm radius, 2 thermograph pixels) enabled accurate image mapping. The wrap was applied at the frustum/tip interface, 102 mm downstream of the sharp nose ($x/L = 0.25$), allowing the boundary layer to develop before the forward-facing step; at this location, the computed boundary-layer thickness at the highest Reynolds number, Re_∞ is 0.55 mm, five times the film thickness. Thermograph temperatures were mapped using a perspective transformation matrix (PTM) (Haralick 1980). As uncertainty propagation through the PTM inversion is impractical, a Monte Carlo simulation was used, giving a mapped-pixel uncertainty of ±0.30 mm. Viewing angles were computed based on camera and model geometry, and a directional emissivity correction was applied.

Heat flux was calculated by solving the transient 1-D heat equation through space and time (Zaccara, Edelman & Cardone 2020). Lateral heat conduction was neglected due to

RETRACTED

https://doi.org/10.1017/jfm.2025.10905

the short test durations, consistent with prior studies showing minimal through-thickness thermal penetration under similar conditions (Rataczak, Running & Juliano 2021; Running *et al.* 2022) The FORTRAN QCALC subroutine was translated to MATLAB® for this purpose (Juliano, Adamczak & Kimmel 2015). QCALC assumes 1-D heat transfer and uses a second-order Euler-explicit finite-difference approximation to solve for the temperature distribution through the wall; heat flux is obtained from a second-order approximation to the derivative of the temperature profile at the outer surface (Boyd & Howell 1994). In this work, a cylindrical coordinate system was used with the local radius of curvature, thickness, and material properties of the vinyl wrap and underlying aluminium wall. The initial condition is based on the assumption of a uniform through-wall temperature distribution, equal to the pre-run surface temperature at each pixel. The measured surface temperature was applied as the front-face boundary condition, and an adiabatic back-face boundary condition was imposed. Radiation was neglected due to relatively low temperatures. The full temperature history, starting from the assumedly isothermal pre-run, was used to solve transient heat conduction and resolve surface heat flux. A 2 h interval between runs ensured thermal equilibrium and consistent initial conditions, preventing residual thermal gradients from affecting the results.

The heat flux was converted to the non-dimensional heat flux, the Stanton number. Throughout this work, a modified Stanton number is used

$$St = \frac{\dot{q}''_{wall}}{c_p \rho_\infty u_\infty (T_0 - T_{wall})}, \tag{3.1}$$

where $\dot{q}''_{wall}$, c_p, ρ_∞, u_∞, T_0 and T_{wall} are the heat flux, specific heat capacity of air at constant pressure, free-stream density, free-stream velocity, stagnation temperature and wall temperature, respectively. The standard heat capacity of air at constant pressure, 1004 J kg^{-1} K^{-1}, was assumed. The uncertainty in St is computed by analysing and propagating the uncertainty associated with each of the parameters in (3.1). The total uncertainty is calculated by taking the square root of the sum of the squares of all uncertainties. The uncertainty range on the Stanton number is $+10/-8$ %. For each test condition, the Stanton number was evaluated during the first steady-flow period after startup transients subsided; it varied minimally despite slight heat-flux changes because the driving temperature difference also decreased.

3.3. *Background-oriented schlieren*

Background-oriented schlieren was used to measure off-wall density-gradient and density fields. The accuracy and precision of the measurement technique for high-speed flows were validated in a previous study (Davami *et al.* 2025*b*). The system included high-resolution and high-speed cameras, a background, and two LED arrays. A Canon EOS RP with 24–105 mm lens recorded 3840 × 2160 pixels at 24 fps to resolve the mean flow, while a Phantom v1840 with a 90 mm Tamron lens recorded 1000 × 100 pixels at 30 000 fps to capture the unsteady dynamics. Depth of field was maximised by using an aperture of $f/22$ (Molnar *et al.* 2024), and measurements were performed simultaneously, with the high-speed camera slightly off-axis.

Two 210 × 297 mm speckled sheets, each with 200 000 randomly distributed 0.25 mm dots, covered the 0.41 m acrylic window and were back illuminated by two LED arrays. With a video resolution of 3840 × 2160 pixels, the dots corresponded to 2.3 pixels in diameter, yielding a density of 321 particles cm^2. Images were analysed in PIVlab (Thielicke & Sonntag 2017) by cross-correlating wind-off and wind-on photographs. The maximum displacement between two images was approximately three pixels, prompting

REFRACTED

https://doi.org/10.1017/jfm.2025.10905

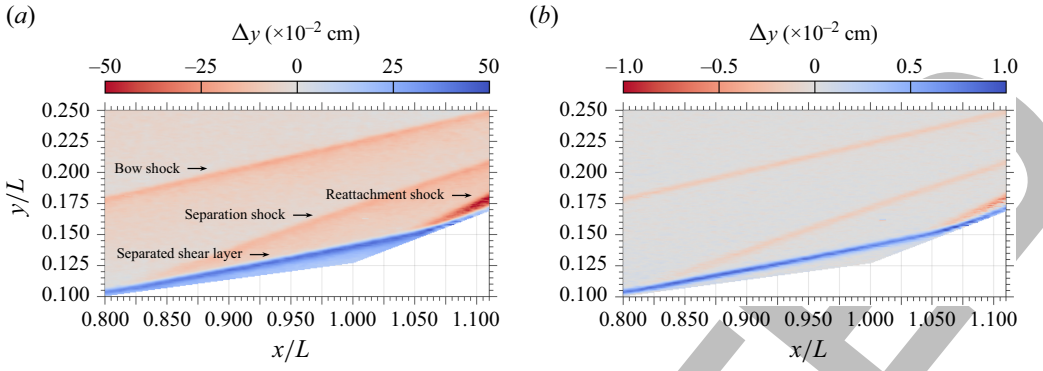


Figure 2. The BOS-measured displacement fields. (*a*) Line-of-sight integrated. (*b*) Centreplane.

the use of a minimum interrogation window size of 8 × 8 pixels as long as sufficiently high correlation values associated with high dot-pattern density allow. A four-pass refinement from 64 × 64 to 8 × 8 pixels with 50 % overlap yielded a 480 × 480 displacement grid at 0.3 mm resolution. To suppress random noise, consecutive displacement fields separated by 0.04 s were averaged.

Optical parameters from the set-up were used to convert from image to physical space, with an uncertainty of ±0.4 mm for a given pixel. Assuming axisymmetry, displacement fields were processed using the filtered back projection technique (FBPT) to reconstruct centreplane gradient fields, from which density was obtained by solving the 2-D Poisson equation (Venkatakrishnan & Meier 2004; Davami *et al.* 2025*b*). Uncertainty quantification followed Rajendran *et al.* (2019), with maximum displacement uncertainty of ±0.026 pixels (±0.15 mm) corresponding to a density uncertainty of ±0.01 kg m^{-3} near shocks. Figure 2(*a*) presents a representative line-of-site-integrated vertical displacement field (Δy), while figure 2(*b*) displays the corresponding FBPT reconstruction on the (axisymmetric) model centreplane. The streamwise and centreline-normal coordinates, x and y, are normalised by the cone length, placing the cone–flare junction at $x/L = 1$. Shock waves appear as large negative Δy, while the shear layer shows positive Δy.

4. Experimental set-up

A schematic of the experimental set-up is shown in figure 3. Infrared thermography and high-resolution, high-speed BOS measurements were collected simultaneously, all on the upper surface of the test article. The IR camera was placed on the top of the tunnel, viewing the model upper surface through a 19 mm thick calcium fluoride (CaF_2) window with a transmission range of 0.15–9.0 μm. The viewing distance was 585 mm. Window absorption was included via camera software using emissivity, ambient temperature and window transmissivity. Calibration with the same window (Running 2020) showed less than 0.2 % difference from thermocouple measurements, indicating that full recalibration is generally unnecessary for comparable experiments.

The cameras used for the BOS measurements were stacked vertically and viewed through a 127 mm diameter acrylic window on the test section left side door (small black circle in figure 3*a*). The viewing distance of the cameras was 600 mm. The BOS background was placed on the other side of the test section, behind a 457 mm diameter acrylic window. The model was installed on a sting that was clamped by a clamshell and bolted to a strut. The strut is bolted onto a baseplate allowing upstream or downstream

https://doi.org/10.1017/jfm.2025.10905

REFRACTED

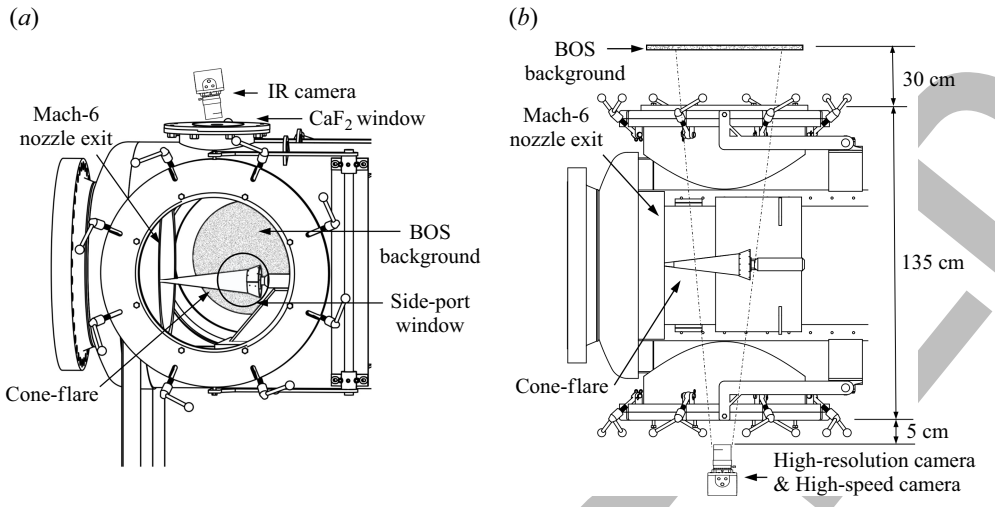


Figure 3. Experimental set-up. (*a*) Side view. (*b*) Top-down view.

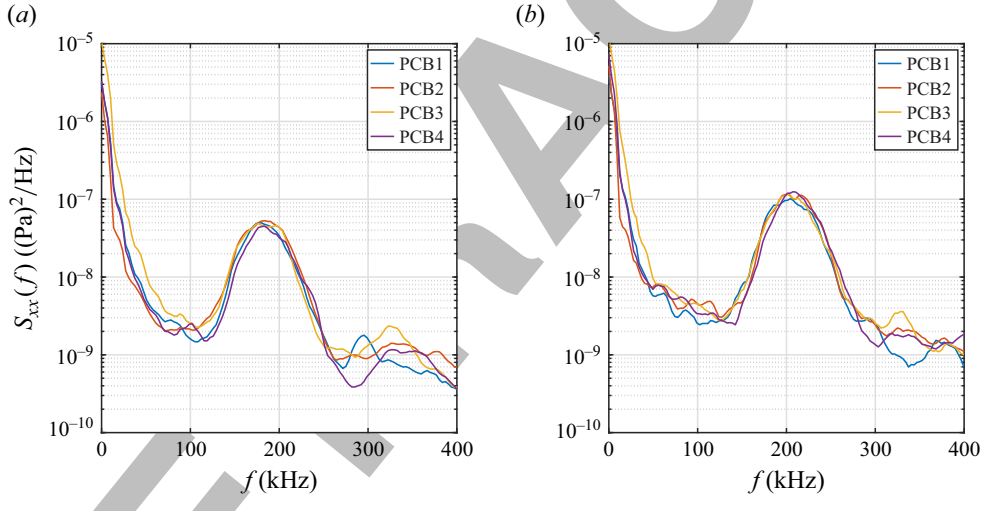


Figure 4. Autospectral densities of PCB-measured pressure fluctuations for $r_n = 0.01$ mm; (*a*) $Re_\infty = 8.4 \times 10^6$ m^{-1}, (*b*) $Re_\infty = 10.0 \times 10^6$ m^{-1}.

movement of the entire assembly. The model nose was positioned 100 mm upstream of the nozzle exit plane.

Alignment with the free-stream flow was established by measuring second-mode pressure fluctuations on the conical forebody. Four PCB132B38 sensors were positioned 88.9 mm upstream of the cone–flare junction at 90° intervals around the azimuth. Second-mode instability waves are the primary transition mechanism for cone geometries at nominally zero angle of attack with sharp noses ($r_n \lesssim 2$ mm (Kennedy *et al.* 2022)), so the sharp nose tip ($r_n = 0.01$ mm) was installed for alignment. Alignment was confirmed when the autospectral density of each PCB exhibited second-mode peaks within 2 % of the mean frequency (Lees & Lin 1947; Benitez *et al.* 2021). Figures 4(*a*) and 4(*b*) illustrate this for $Re_\infty = 8.4 \times 10^6$ and 10.0×10^6 m^{-1}. Based on the last adjustment made, both pitch and yaw alignment are within $0.0 \pm 0.1°$. In high-speed facilities, achieving alignment at

https://doi.org/10.1017/jfm.2025.10905

a specific Re_∞ does not guarantee alignment at others (Davami *et al.* 2023*a*; Leidy *et al.* 2024; Benitez *et al.* 2024*b*; Leidy *et al.* 2025). The excellent agreement in the second-mode peak frequencies at each azimuth indicates the flow angularity in the ANDLM6QT is consistent, at least within this Re_∞ range.

5. Computational methodologies and results

Computational investigations of the flare-induced SWBLI were conducted using the same cone–flare geometry at matching conditions. Fixed-point and shock-adapted laminar and turbulent base flows were computed. Stability analysis was performed using a hybrid methodology combining parabolised stability equations (PSE) and harmonic linearised Navier–Stokes equations (HLNSE) solutions, alongside GSA of the laminar axisymmetric separation bubble. Direct numerical simulations were also carried out for comparison with GSA and experimental results.

5.1. *Laminar and turbulent base flows*

The presented results were computed for the cone–flare test article for all three nose radii, using a grid of 2201×826 points along the streamwise and wall-normal directions, respectively. Figure 5 is a representative grid, for $r_n = 0.99$ mm and adapted to $Re_\infty = 5.8 \times 10^6$ m^{-1}. The nose region is shown with every other streamwise line and every twentieth wall-normal point; the full geometry is shown with every tenth line in both directions. The laminar flow solutions were computed with a second-order accurate algorithm as implemented in the finite-volume compressible Navier–Stokes flow solver VULCAN-CFD (visit http://vulcan-cfd.larc.nasa.gov for further information about the VULCAN-CFD solver) (Baurle & Edwards 2020). The VULCAN-CFD solution is based on the full Navier–Stokes equations and uses the solver's built-in capability to iteratively adapt the computational grid to the bow shock and boundary layer (Scholten *et al.* 2022; Scholten 2024). Adaptation ensures enough points are clustered next to the model surface to resolve the thickness of the boundary layer within the separation region. For this process, the boundary-layer edge is defined as the wall-normal position where $h_0/h_{0,\infty} = 0.99$, with h_0 denoting the total enthalpy, i.e. $h_0 \equiv h + (1/2)(\bar{u}^2 + \bar{v}^2 + \bar{w}^2)$, where $h = c_p \bar{T}$ is the static enthalpy. An offset is also applied and ensures the chosen number of cells in the wall-normal direction will properly resolve the entropy layer as well. Sutherland's law for air is used to calculate the dynamic viscosity as a function of temperature. An isothermal wall with $T_w = 290$ K is used and free-stream conditions were selected to replicate most of the experimental runs (table 2).

Figure 6 presents Mach number contours of two representative laminar basic-state solutions for nose radius $r_n = 0.1$ mm, illustrating the effect of Re_∞ on the topology of the SWBLI. The upper Mach number contour is for $Re_\infty = 5.8 \times 10^6$ m^{-1}, while the lower is $Re_\infty = 10.1 \times 10^6$ m^{-1}. The separation and reattachment locations are denoted by '$\circ$'. As Re_∞ increases, the laminar boundary layer on the conical forebody becomes less resistant to separation, resulting in earlier separation for $Re_\infty = 10.1 \times 10^6$ m^{-1} than for $Re_\infty = 5.8 \times 10^6$ m^{-1}. Despite different separation locations, the reattachment location is nearly identical for both Re_∞.

Figure 7 presents the effect of nose radius on the laminar SWBLI for $Re_\infty = 5.8 \times 10^6$ m^{-1}. The Mach number contour for the upper domain is for $r_n = 0.1$ mm, while the lower is for $r_n = 5.0$ mm. The differences in x_s/L and x_r/L are slightly exaggerated between the upper and lower contours due to the shorter cone length for $r_n = 5.0$ mm, which is 36 mm shorter. Nevertheless, as the nose radius increases, the

RETRACTED

https://doi.org/10.1017/jfm.2025.10905

Re_∞ ($\times 10^6$ m^{-1})	u_∞ (m s^{-1})	ρ_∞ (kg m^{-3})	T_∞ (K)	T_0 (K)	T_{wall} (K)	P_0 ($\times 10^6$ Pa)
5.8	870.35	0.0255	58.02	435	290	0.4901
7.6	870.35	0.0334	58.02	435	290	0.6421
8.5	870.35	0.0374	58.02	435	290	0.7182
10.1	870.35	0.0444	58.02	435	290	0.8534
12.1	870.35	0.0532	58.02	435	290	1.0224

Table 2. Computational flow conditions.

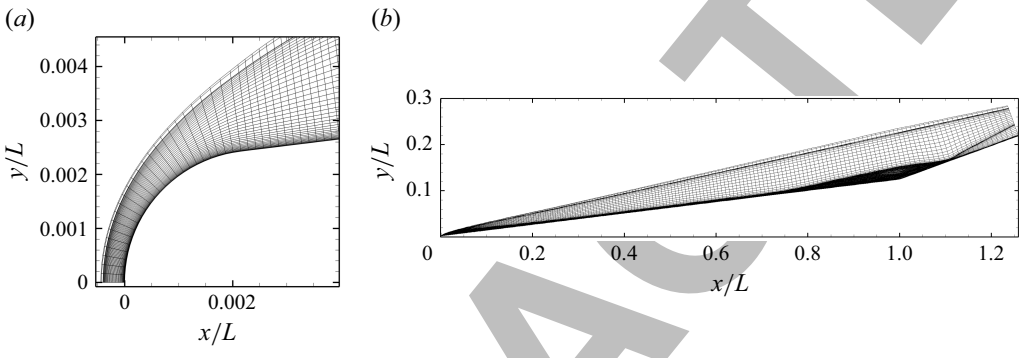


Figure 5. An $r_n = 0.99$ mm grid adapted to $Re_\infty = 5.8 \times 10^6$ m^{-1}. (a) Nose region, (b) Full geometry.

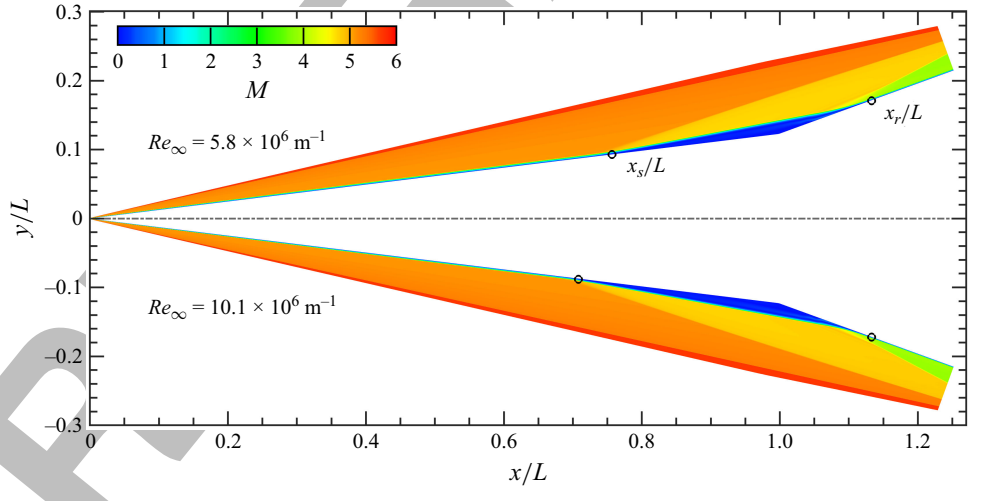


Figure 6. Effect of Re_∞ on the laminar SWBLI ($r_n = 0.01$ mm).

boundary layer on the conical forebody is thicker, and the edge Mach number decreases. This leads to earlier separation, later reattachment, and increased separation bubble length. Additionally, a blunter nose results in a thicker entropy layer on the cone, influencing the development of instabilities (Paredes *et al.* 2019*b*; Kennedy *et al.* 2022). The separation bubble properties are tabulated in table 3 for all laminar conditions computed.

https://doi.org/10.1017/jfm.2025.10905

r_n (mm)	Re_∞ ($\times 10^6$ m^{-1})	x_s (m)	x_s/L	x_r (m)	x_r/L	l_s (m)	l_s/L	$\max(-u)/u_\infty$
0.01	5.8	0.3105	0.7506	0.4639	1.1212	0.1534	0.3709	0.2284
0.01	7.6	0.3006	0.7267	0.4640	1.1214	0.1634	0.3950	0.2504
0.01	8.5	0.2965	0.7170	0.4639	1.1212	0.1674	0.4048	0.2596
0.01	10.1	0.2912	0.7041	0.4635	1.1203	0.1723	0.4166	0.2728
0.01	12.1	0.2850	0.6893	0.4632	1.1197	0.1783	0.4311	0.2864
0.99	5.8	0.3025	0.7442	0.4580	1.1273	0.1555	0.3825	0.2291
0.99	7.6	0.2920	0.7183	0.4582	1.1278	0.1663	0.4091	0.2513
0.99	8.5	0.2879	0.7083	0.4581	1.1276	0.1702	0.4185	0.2611
0.99	10.1	0.2821	0.6941	0.4578	1.1267	0.1757	0.4321	0.2742
0.99	12.1	0.2752	0.6771	0.4577	1.1265	0.1825	0.4490	0.2878
5.00	5.8	0.2036	0.5390	0.4519	1.1961	0.2483	0.6572	0.2634
5.00	7.6	0.1747	0.4624	0.4547	1.2035	0.2800	0.7411	0.2902
5.00	8.5	0.1592	0.4214	0.4562	1.2074	0.2969	0.7860	0.3015
5.00	10.1	0.1296	0.3430	0.4584	1.2134	0.3289	0.8705	0.3194
5.00	12.1	0.0846	0.2240	0.4601	1.2179	0.3755	0.9939	0.3401

Table 3. Separation bubble properties for all nose radii and Reynolds numbers.

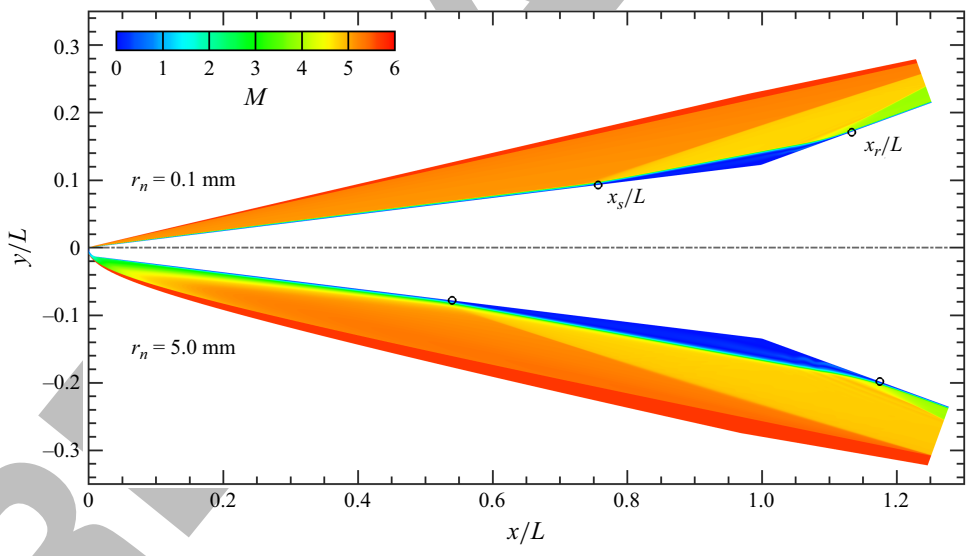


Figure 7. Effect of r_n on the laminar SWBLI ($Re_\infty = 5.8 \times 10^6$ m^{-1}).

In addition to the laminar solutions, fully turbulent solutions were computed at the same free-stream Reynolds numbers using the Menter-Shear stress transport (SST) Reynolds-averaged Navier–Stokes (RANS) turbulence model (Menter 1994) to compare with experimental results. Additional details of the implementation of the model in the VULCAN-CFD solver are found in Baurle & Edwards (2020).

REJECTED

https://doi.org/10.1017/jfm.2025.10905

5.2. *Stability analysis*

The methodologies used for the analysis of disturbance amplification are equivalent to those used by Paredes *et al.* (2022). The evolution of convective instabilities was calculated with the linear PSE and the HLNSE frameworks. Global stability analysis of the laminar flow solution was also performed.

The Cartesian coordinates are represented by (x, y, z). The computational coordinates are defined as an orthogonal body-fitted coordinate system along the cone, with (ξ, η, ζ) denoting the wall-parallel ('streamwise'), wall-normal and azimuthal coordinates, respectively, and (u, v, w) representing their corresponding velocity components. The same orientation of the coordinate system and velocities is maintained along the flare with a non-orthogonal transformation of the two-dimensional grid. The density and temperature are denoted by ρ and T, respectively. The vector of basic-state variables is $\bar{\boldsymbol{q}}(\xi, \eta, \zeta) = (\bar{\rho}, \bar{u}, \bar{v}, \bar{w}, \bar{T})^\top$ and the vector of perturbation variables is denoted by $\tilde{\boldsymbol{q}}(\xi, \eta, \zeta, t) = (\tilde{\rho}, \tilde{u}, \tilde{v}, \tilde{w}, \tilde{T})^\top$. For axisymmetric geometries at zero degrees angle of attack, the basic-state variables are independent of the azimuthal coordinate and the linear perturbations can be assumed to be harmonic in time and in the azimuthal direction, which leads to the following expression for the perturbations

$$\tilde{\boldsymbol{q}}(\xi, \eta, \zeta, t) = \breve{\boldsymbol{q}}(\xi, \eta) \exp\left[\mathrm{i}\,(m\zeta - \omega t)\right] + \text{c.c.}, \tag{5.1}$$

where the vector of disturbance functions is $\breve{\boldsymbol{q}}(\xi, \eta) = (\breve{\rho}, \breve{u}, \breve{v}, \breve{w}, \breve{T})^\top$, m is the azimuthal wavenumber, ω is the angular frequency and c.c. refers to the complex conjugate.

The disturbance functions $\breve{\boldsymbol{q}}(\xi, \eta, \zeta)$ satisfy the HLNSE (Paredes *et al.* 2019*a*), which involve coefficient functions that depend on the basic-state variables and parameters, and on the angular frequency and azimuthal wavenumber of the perturbation

$$\boldsymbol{L}_{HLNSE}\, \breve{\boldsymbol{q}}(\xi, \eta) = \breve{\boldsymbol{f}}, \tag{5.2}$$

where $\breve{\boldsymbol{f}}$ represents a potential forcing term.

The PSE approximation to the HLNSE is based on isolating the rapid phase variations in the streamwise direction by introducing the disturbance ansatz

$$\breve{\boldsymbol{q}}(\xi, \eta, \zeta) = \hat{\boldsymbol{q}}(\xi, \eta, \zeta) \exp\left[\mathrm{i} \int_{\xi_0}^{\xi} \alpha(\xi')\, \mathrm{d}\xi'\right], \tag{5.3}$$

where the unknown, streamwise-varying wavenumber $\alpha(\xi)$ is determined in the course of the solution by imposing an additional constraint

$$\int_\eta \hat{\boldsymbol{q}}^* \frac{\partial \hat{\boldsymbol{q}}}{\partial \xi}\, h_\xi\, h_\zeta\, \mathrm{d}\eta\, \mathrm{d}\zeta = 0, \tag{5.4}$$

and requiring the amplitude functions $\hat{\boldsymbol{q}}(\xi, \eta, \zeta) = (\hat{\rho}, \hat{u}, \hat{v}, \hat{w}, \hat{T})^\top$ to vary slowly in the streamwise direction in comparison with the phase term $\exp[\mathrm{i} \int_{\xi_0}^{\xi} \alpha(\xi')\, \mathrm{d}\xi']$. Substituting (5.3) into the HLNSE and invoking scale separation between the streamwise coordinate and the other two directions to neglect the viscous terms with streamwise derivatives, the PSE are obtained in the form

$$\left(\boldsymbol{L}_{PSE} + \boldsymbol{M}_{PSE} \frac{1}{h_\xi} \frac{\partial}{\partial \xi}\right) \hat{\boldsymbol{q}}(\xi, \eta) = 0. \tag{5.5}$$

The onset of laminar-turbulent transition is estimated by using the logarithmic amplification ratio, the so-called N-factor, relative to the location ξ_I where the disturbance

RETRACTED

https://doi.org/10.1017/jfm.2025.10905

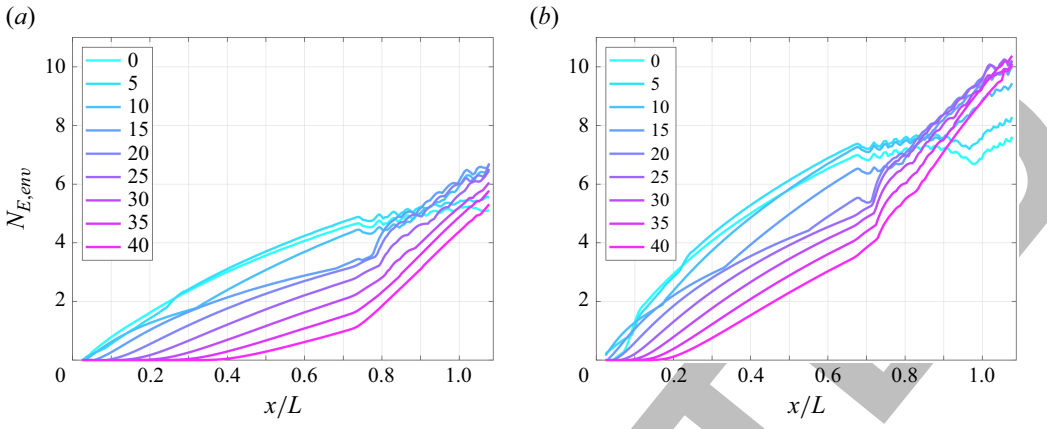


Figure 8. Evolution of N-factor envelopes based on total disturbance energy ($N_{E,env}$). Legend reflects the different azimuthal wavenumbers; (*a*) $Re_\infty = 5.8 \times 10^6$ m^{-1}, (*b*) $Re_\infty = 12.1 \times 10^6$ m^{-1}.

first becomes unstable

$$N_\phi = -\int_{\xi_I}^{\xi} \alpha_i(\xi')\,\mathrm{d}\xi' + \ln\left[\hat{\phi}(\xi)/\hat{\phi}(\xi_I)\right]. \tag{5.6}$$

Here, $\hat{\phi}$ denotes an amplitude norm of $\hat{\boldsymbol{q}}$ at a given ξ, e.g. wall-pressure disturbance or total disturbance energy E (Chu 1956; Mack 1969).

The evolution of convective boundary-layer instabilities is analysed with a hybrid methodology comprising PSE and HLNSE solutions across overlapping streamwise domains. The linear amplification of planar and oblique, first and second Mack mode disturbances along the cone, is computed with PSE until just upstream of the cone–flare corner. The HLNSE is used to calculate the development of the instability waves through the remaining length of the geometry. Figure 8 shows the comparison of the N-factor envelopes based on the total disturbance energy for the planar and oblique waves with different azimuthal wavenumbers shown by the legend, for the lowest and highest free-stream Reynolds numbers. The effect of a lower Reynolds number is to reduce the amplification of the disturbances. At the separation location around $x/L \approx 0.75$ ($x \approx 0.31$ m), an N-factor of ≈4.88 is predicted for $Re_\infty = 7.6 \times 10^6$ m^{-1}, while a higher $N_E \approx 7.46$ is found for $Re_\infty = 10.1 \times 10^6$ m^{-1}. Experimental measurements indicate the boundary layer is laminar upstream of separation, thus these amplification factors are not sufficient to lead to transition onset.

The GSA is based on the HLNSE, with the real-valued angular frequency ω from (5.1) replaced by a complex value $\Omega = \omega + \mathrm{i}\sigma$, where σ is the temporal growth rate of the disturbance. After setting $\breve{\boldsymbol{f}} = 0$ and defining $\hat{\boldsymbol{q}} \equiv \breve{\boldsymbol{q}}$, (5.2) can be written as the generalised eigenvalue problem

$$\boldsymbol{A}\hat{\boldsymbol{q}} = \Omega \boldsymbol{B}\hat{\boldsymbol{q}}, \tag{5.7}$$

where the leading eigenvalues Ω and eigenvectors $\hat{\boldsymbol{q}}$ are calculated with the Arnoldi algorithm (Saad 1980).

Grid sensitivity was analysed for $Re_\infty = 12.1 \times 10^6$ m^{-1} at all nose radii using different grid resolution for the computation of the laminar basic state. For each grid, the solution was used to compute the azimuthal wavenumber and growth rate associated with the maximum global instability (table 4). The relative differences between the azimuthal wavenumbers associated with the maximum growth rate between the 2001 × 751 and

RETRACTED

https://doi.org/10.1017/jfm.2025.10905

r_n (mm)	Resolution	m_{max}	σ_{max} (1/ms)
0.01	2001 × 751	76.22	31.05
0.01	2201 × 826	71.20	30.48
0.01	2401 × 901	69.76	30.40
0.99	2001 × 751	70.51	30.03
0.99	2201 × 826	70.66	30.56
0.99	2401 × 901	69.17	30.25
5	2001 × 751	65.45	30.24
5	2201 × 826	63.93	29.25
5	2401 × 901	62.37	28.34

Table 4. Wavenumber associated with the most unstable global disturbance using different basic-state grid resolutions at $Re_\infty = 12.1 \times 10^6$ m^{-1}.

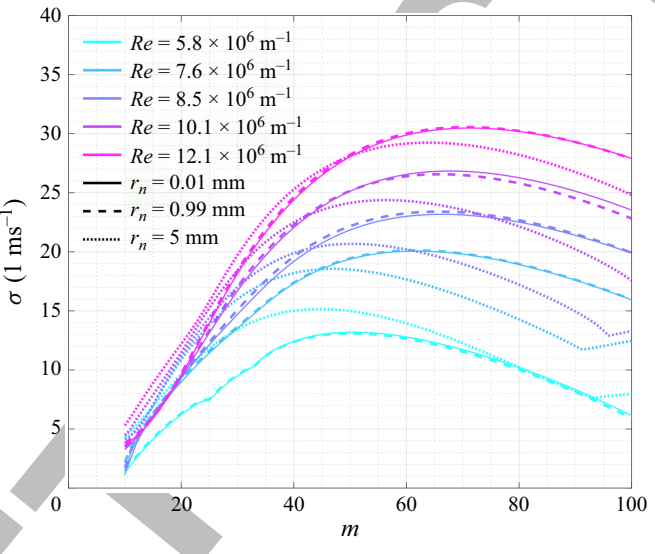


Figure 9. Leading instability growth rate from GSA as function of wavenumber, Re_∞, and r_n.

2401 × 901 grids are under 10 %, and the lower Re_∞ cases have lower relative differences. Therefore, this worst case justifies the 2201 × 826 grid be used for the computation of all basic states.

The leading global instability growth rate at each of the selected conditions given in table 2 is shown in figure 9. For all Reynolds numbers computed, the flow was globally unstable. The leading unstable mode is a short-wavelength stationary disturbance with wavenumber increasing from $m = 50$ to $m = 71$ as the Reynolds number increases. The eigenspectra computed for the lowest Reynolds number is given in figure 10 for all three nose radii. Oscillatory mode families exist but remain less amplified than the dominant, stationary, mode. The eigenspectrum remains relatively similar between $r_n = 0.1$ and $r_n = 0.99$ mm. For the largest nose radius, additional oscillatory modes become unstable.

The real part of the azimuthal velocity component of the corresponding global mode eigenfunctions for the lowest and highest Reynolds numbers for the 1 mm tip at peak

REJECTED

https://doi.org/10.1017/jfm.2025.10905

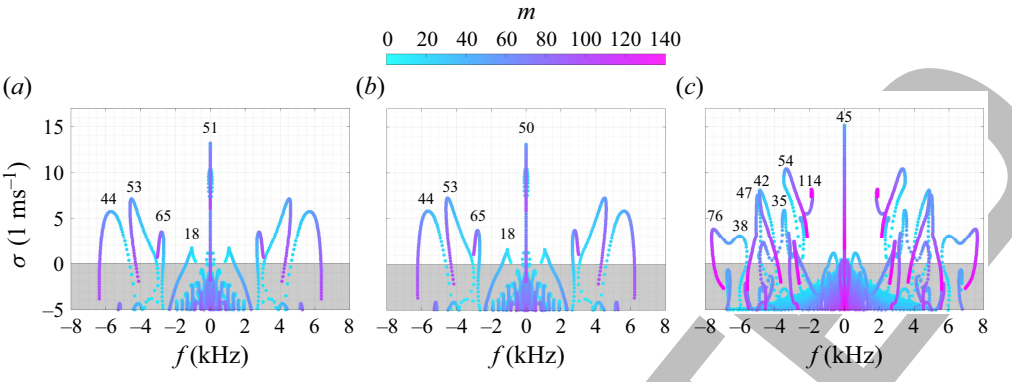


Figure 10. Eigenspectra obtained by GSA for $Re_\infty = 5.8 \times 10^6$ m^{-1}. The grey area indicates stable eigenvalues. The wavenumber at the peaks is given by the number near each one; (*a*) $r_n = 0.1$ mm, (*b*) $r_n = 0.99$ mm, (*c*) $r_n = 5$ mm.

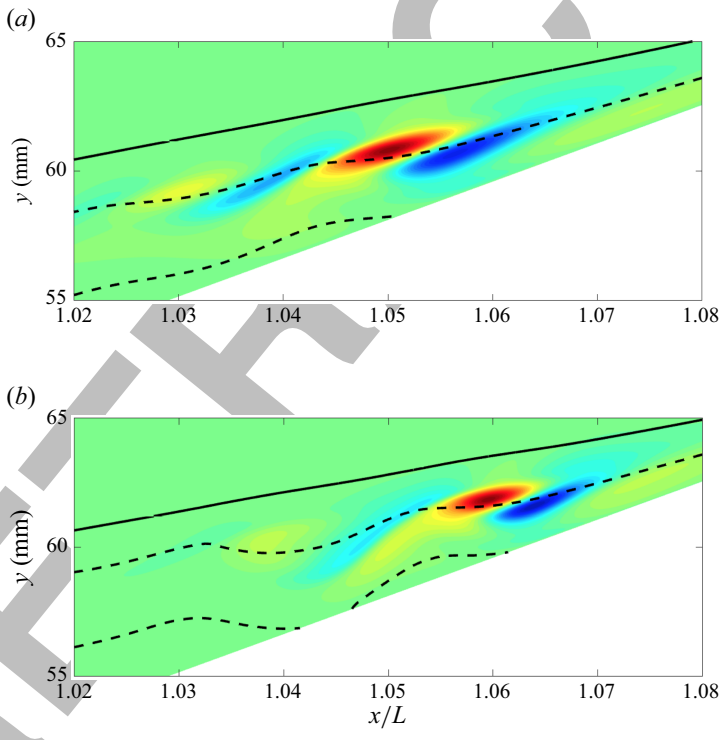


Figure 11. Real part of streamwise-velocity perturbation corresponding to the leading disturbance as computed by GSA ($r_n = 0.99$ mm): (*a*) $Re_\infty = 5.8 \times 10^6$ m^{-1} and $m = 50$; (*b*) $Re_\infty = 12.1 \times 10^6$ m^{-1} and $m = 70$.

growth rates are presented in figure 11. The boundary-layer edge is displayed for each mode shape as a solid black line and, unlike in the grid adaptation process, is defined more precisely by $h_0/h_{0,\infty} = 0.995$. In addition, the first and second separation regions are shown by dashed black lines at $u = 0$. This short-wavelength mode is concentrated at the reattachment location with no significant presence at the corner. It straddles the separation line of the first, larger, separated region.

https://doi.org/10.1017/jfm.2025.10905

5.3. *Direct numerical simulations*

Direct numerical simulations were performed for $r_n = 0.99$ mm at $Re_\infty = 5.8 \times 10^6$ m^{-1} and 7.6×10^6 m^{-1} to compare with experiment and GSA, and to characterise the nonlinear behaviour of the finite-amplitude global modes and their effect on the formation of thermal striations along the flare.

To simulate the boundary-layer flow by DNS, the full, 3-D, compressible Navier–Stokes equations in conservation form were solved numerically in cylindrical coordinates. The working fluid is air and falls within the perfect gas regime. The usual constitutive relations for a Newtonian fluid were used: the viscous stress tensor is linearly related to the rate-of-strain tensor, and the heat-flux vector is linearly related to the temperature gradient through Fourier's law. The coefficient of viscosity μ is computed from Sutherland's law, and the coefficient of thermal conductivity κ is computed from $\kappa = \mu C_p/Pr$, with a molecular Prandtl number of $Pr = 0.72$. The inviscid fluxes of the governing equations were computed using a seventh-order weighted essentially non-oscillatory (WENO) scheme (Jiang & Shu 1996). The viscous fluxes were discretised using a fourth-order central-difference scheme, and time integration was performed using a third-order, low-storage, Runge–Kutta scheme (Williamson 1980). A similar WENO-based numerical solver has been successfully applied to study hypersonic transitional flows including transitional SWBLIs over a compression ramp at Mach 7.7 (Cao *et al.* 2021) and a cone–cylinder–flare model at Mach 6 (Li *et al.* 2024).

To set up the DNS, the unperturbed boundary-layer flow and axisymmetric separation bubble computed with the VULCAN-CFD flow solver were used to obtain a shock-adapted solution for the entire cone–flare model. Then a subset of the computational domain of $x/L = [0.367, 1.258]$ that covers the separation and reattachment regions was used for the DNS with the same grid distribution. Figure 12(*a*) visualises the DNS subdomain along with the full-domain VULCAN-CFD solution along a meridional plane for the DNS case at $Re_\infty = 5.8 \times 10^6$ m^{-1}. Here, the inflow of the DNS domain is placed significantly upstream of the cone–flare junction to allow for inflow adjustment and guarantee adequate decay of any instabilities from the inflow boundary so that the global instabilities from the separation bubble can be isolated. The DNS domain extends in the wall-normal direction from the cone surface to just below the bow shock. The inflow and the upper boundary conditions for the DNS were obtained by using the VULCAN-CFD solution. An unsteady, non-reflecting boundary condition based on Thompson (1987) is used at the outflow boundary. For the no-slip wall, isothermal conditions are specified with the wall temperature of $T_w = 290$ K.

For each Reynolds number, a steady simulation with a 2-D subdomain of $x/L = [0.367, 1.258]$, referred to as 2-D DNS, was first performed and validated against the full-domain VULCAN-CFD solution. Next, the 2-D domain of 2-D DNS was extruded along the azimuthal direction with a spanwise extent of ϕ, and a 3-D unsteady simulation with periodic boundary conditions in the spanwise direction was performed, referred to as 3-D DNS (figure 12*b*). Both the 2-D and 3-D DNS runs use a total number of grid points of $N_x = 740$ and $N_r = 540$ in the streamwise and radial directions, respectively. The spanwise extent of the primary 3-D DNS was selected to be $\phi = 90°$ (corresponding to an azimuthal wavenumber $m = 4$), wide enough to accommodate multiple thermal streaks within the domain. A total of $N_\phi = 800$ points were used.

For each case, the 3-D DNS was initialised with no disturbances inside the domain or at the boundaries. As demonstrated in Cao *et al.* (2021) and Li *et al.* (2024), the growth of instability waves can arise from the extremely low-level perturbations provided by numerical round-off error, which enables the examination of intrinsic instabilities

REJECTED

https://doi.org/10.1017/jfm.2025.10905

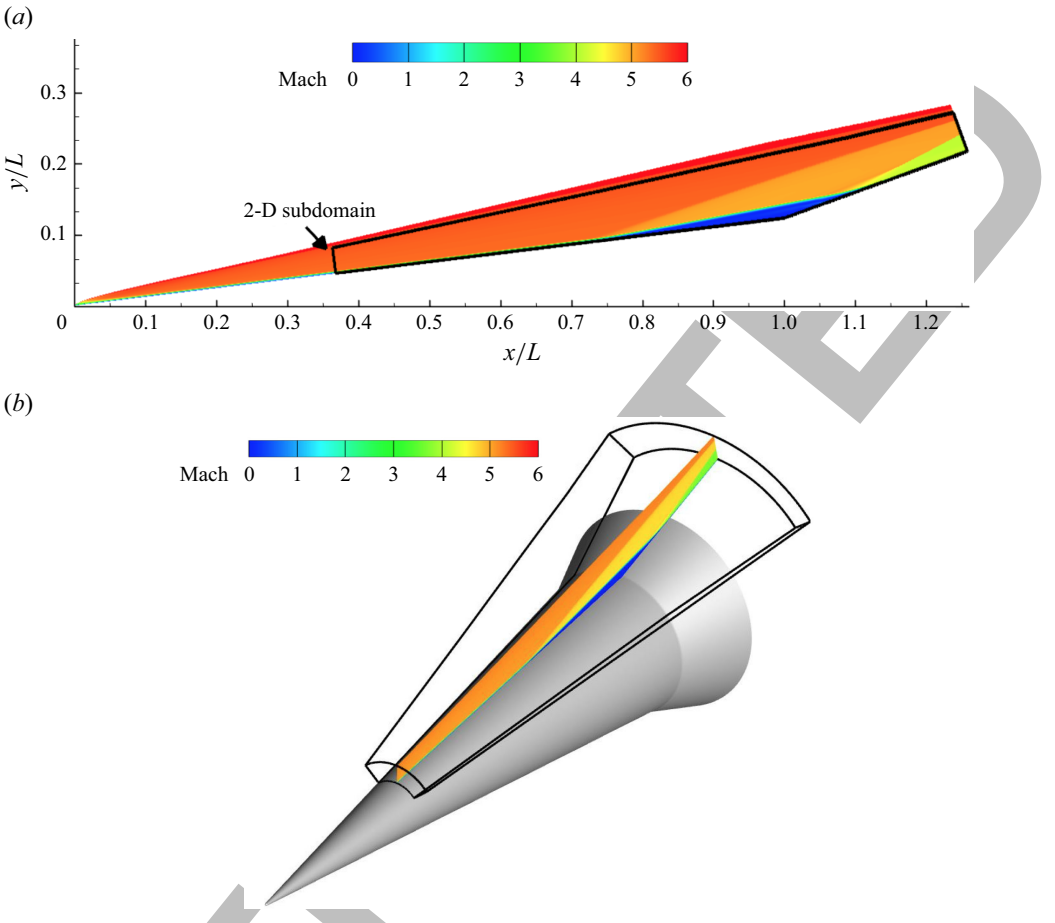


Figure 12. The DNS subdomain along with full-domain basic-state Mach number contours computed by VULCAN-CFD ($r_n = 0.99$ mm and $Re_\infty = 5.8 \times 10^6$ m^{-1}); (*a*) 2-D DNS, (*b*) 3-D DNS $m = 4$.

in the fluid-dynamic system. The 3-D DNS was run with a constant time step of $\Delta t = 1.2$ ns for at least 5.7 ms. A fully developed flow field was established within $t \approx 1.40$ ms for $Re_\infty = 5.8 \times 10^6$ m^{-1} and $t \approx 1.0$ ms for $Re_\infty = 7.6 \times 10^6$ m^{-1}. These values were determined by monitoring the exponential temporal growth and saturation of the spanwise-velocity fluctuations within the separation bubble, which is shown later.

Table 5 summarises the DNS cases along with the spatial and temporal parameters. N_x, N_ϕ and N_r are the number of grid points in the streamwise, azimuthal and radial directions, respectively. Here, Δx_s is the streamwise wall-parallel grid spacing, $(r\Delta\phi)_w^+$ is the azimuthal grid spacing at the wall and $\Delta y_{n,w}$ is the wall-normal grid spacing at wall. The superscript '+' denotes normalisation by the viscous length near the end of the DNS domain at $x/L = 1.13$. The selection of grid and other aspects of the numerical solution were based on extensive experience with a similar class of flows, including independent verification of the DNS tools against multiple solvers from different computational groups for the scaled ROTEX-T cone–flare geometry (Davami *et al.* 2025*c*). Additional assessment of the grid resolution for the DNS is included in Appendix A.

Table 6 compares the properties of the separation bubble between the 2-D DNS baseflow, 3-D DNS and VULCAN-CFD solutions. Excellent agreement is achieved between 2-D DNS and VULCAN-CFD, indicating the validity of the laminar base

https://doi.org/10.1017/jfm.2025.10905

Case	Re_∞ ($\times 10^6$ m^{-1})	ϕ (°)	$N_x \times N_\phi \times N_r$	t (ms)	Δx_s^+	$(r\Delta\phi)^+$	$\Delta y_{n,w}^+$
Re5.8	5.8	90	740 × 800 × 540	[1.4, 6.6]	11.2	2.50	0.046
Re7.6	7.6	90	740 × 800 × 540	[1.0, 5.7]	23.0	5.13	0.080

Table 5. Summary of DNS cases along with spatial and temporal parameters.

Case	Code	x_s (m)	x_s/L	x_r (m)	x_r/L	l_s (m)	l_s/L	$\max(-u)/u_\infty$
Re5.8	VULCAN-CFD	0.3025	0.7442	0.4580	1.1273	0.1555	0.3825	0.2291
	2-D DNS	0.3019	0.7426	0.4582	1.1268	0.1562	0.3842	0.2212
	3-D DNS	0.2941	0.7233	0.4595	1.1300	0.1686	0.4148	0.1171
Re7.6	VULCAN-CFD	0.2920	0.7183	0.4582	1.1278	0.1663	0.4091	0.2513
	2-D DNS	0.2917	0.7175	0.4582	1.1269	0.1665	0.4094	0.2435
	3-D DNS	0.2844	0.6995	0.4560	1.1215	0.1747	0.4297	0.1062

Table 6. Computed separation bubble properties for $r_n = 0.99$ mm.

flow computed by the DNS code. Very small differences are seen in separation and reattachment locations and the size of the separation bubble between the laminar base flow and the averaged mean flow of the 3-D DNS, indicating that the flare boundary layer remains laminar. Nevertheless, the finite-amplitude global modes cause an appreciable deviation in the normalised maximum reverse velocity from the laminar base flow.

To monitor the initial growth of instability waves arising from the extremely low-level perturbations provided by numerical round-off error and the subsequent saturation and establishment of 3-D flow for each 3-D DNS case, we follow the approach by Cao *et al.* (2021) and consider the temporal evolution of the quadratic mean of the spanwise velocity at a streamwise position, which is defined as

$$A_w \equiv \sqrt{\frac{1}{N_r N_\phi} \sum_{j=1}^{N_\phi} \sum_{k=1}^{N_r} (w/U_\infty)_{j,k}^2}, \tag{5.8}$$

where w is the azimuthal velocity, U_∞ is the free-stream velocity and N_ϕ and N_r are the number of grid points in the azimuthal and radial directions, respectively. Figure 13 shows the time evolution of A_w inside the separation bubble near reattachment ($x/L = 1.05$) for both 3-D DNSs. The round-off errors of the order of $A_w = 10^{-7}$ at the very beginning start to grow exponentially at $t \approx 1.0$ and 0.7 ms, respectively, for $Re_\infty = 5.8 \times 10^6$ and $Re_\infty = 7.6 \times 10^6$ m^{-1}, until reaching the asymptotic level of $A_w = 10^{-2}$ at $t \approx 1.4$ and 1.0 ms at each Reynolds number, which marks the start of the 'saturated' regime. The black dashed and dash-dotted lines represent the maximum growth rate predicted by GSA, 13.1 ms^{-1} for $Re_\infty = 5.8 \times 10^6$ m^{-1} and 20.1 ms^{-1} for $Re_\infty = 7.6 \times 10^6$ m^{-1}. The comparison of exponential instability growth from DNS data matches the maximum growth rates predicted by the GSA extremely well, suggesting that the global instability of the recirculation bubble is the primary cause of 3-D flow structures such as reattachment streaks.

RETRACTED

https://doi.org/10.1017/jfm.2025.10905

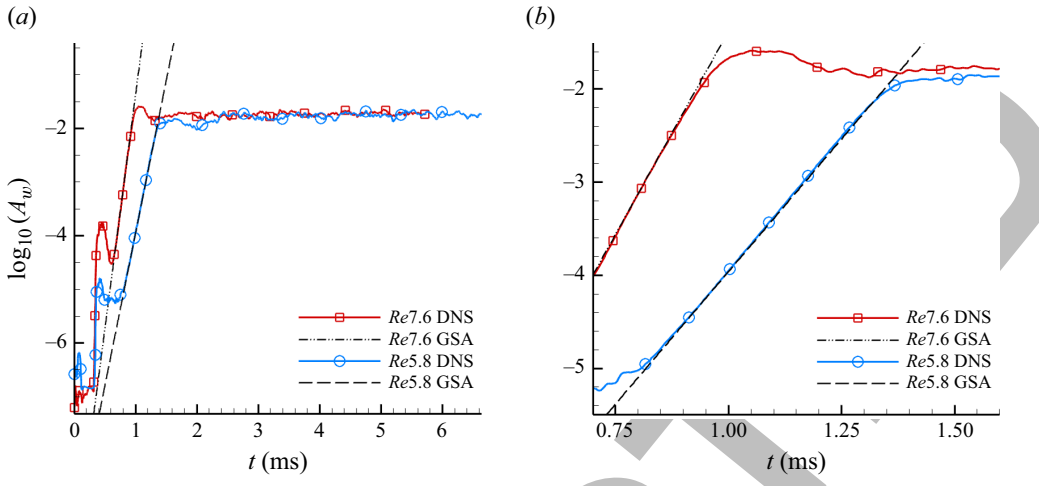


Figure 13. The DNS instability growth measured by A_w (5.8) near reattachment ($x/L = 1.05$). (*a*) Full time series. (*b*) Linear growth regime.

To assess the flow state in the DNS, the temporal evolution of spanwise-averaged surface Stanton number (St) is presented in figure 14 for $Re_\infty = 5.8 \times 10^6$ and 7.6×10^6 m^{-1}, with $r_n = 0.99$ mm. The temporal evolution of spanwise-averaged separation (leftmost black line) and reattachment (rightmost black line) locations are also provided, determined as the location where $\tau_w = 0$, while neglecting the few locations within the separation bubble where τ_w reaches zero but does not indicate reattachment. The standard deviations of $x_s(t)$ and $x_r(t)$ about their mean, indicating the extent of the intermittent region, are $\sigma_s = 2.8$ mm, $\sigma_r = 1.3$ mm at $Re_\infty = 5.8 \times 10^6$ m^{-1}, and $\sigma_s = 2.5$ mm, $\sigma_r = 1.5$ mm at $Re_\infty = 7.6 \times 10^6$ m^{-1}. At both Reynolds numbers, saturation of the global instabilities causes a slight upstream shift of the separation location over time, whereas the average reattachment location remains essentially stationary, leading to an overall enlargement of the separation bubble. Large intermittent spurts of St near reattachment are apparent once the flow saturates (horizontal red dashed line) – St almost doubles compared with the linear growth regime. Although the reattachment location is nearly identical for both Re_∞ (0.04 % difference), the magnitude of heating spurts increases significantly. A movie of the temporal evolution of surface heating is provided in the supplementary movie is available at https://doi.org/10.1017/jfm.2025.10905.

The DNS flow state is further assessed in figure 15, which presents streamwise Stanton number profiles from the 3-D DNS (time/spanwise averaged) alongside laminar and turbulent VULCAN-CFD predictions for $Re_\infty = 5.8 \times 10^6$ and 7.6×10^6 m^{-1} for $r_n = 0.99$ mm. Over the flare, the 3-D DNS exhibits St values higher than the laminar base flow, yet substantially lower than those predicted by the turbulent RANS solution. Nonlinear saturation of the unstable global modes within the recirculation bubble leads to increased peak heating on the flare (Davami *et al.* 2025*c*). Given that Menter's SST model provides a reasonable estimate of turbulent heating on the flare, these comparisons indicate that the 3-D DNS remains laminar along the conical forebody but reaches the onset of transition at reattachment, with intermittent turbulent bursts – some exceeding $St = 3.5 \times 10^{-3}$, comparable to the RANS-predicted turbulent levels – as evidenced in figure 14(*b*).

Figure 16 presents time-averaged skin-friction coefficient ($C_f \equiv \tau_w/((1/2)\rho_\infty u_\infty^2)$) distributions from DNS. Separation is identified by C_f changing from positive to negative,

https://doi.org/10.1017/jfm.2025.10905

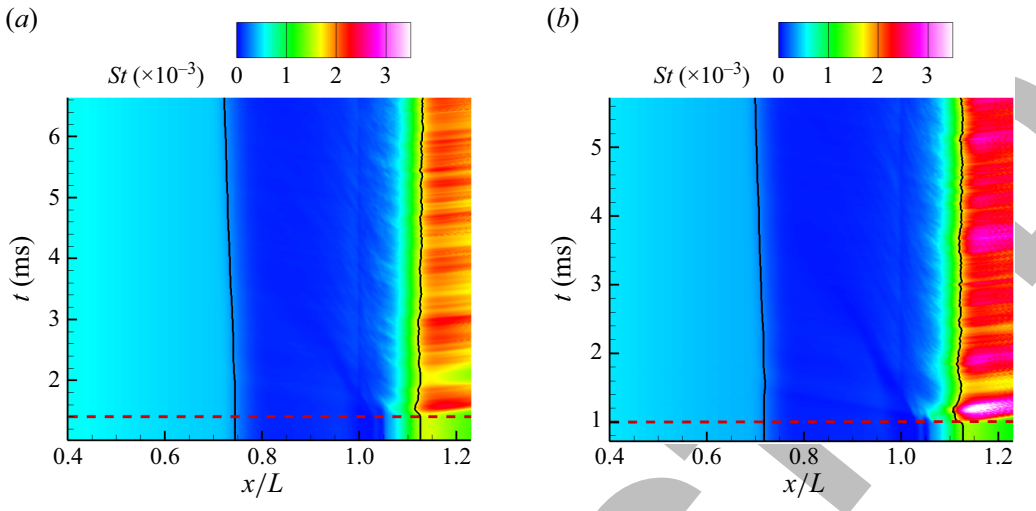


Figure 14. The DNS results of the temporal evolution of Stanton number ($r_n = 0.99$ mm). (*a*) $Re_\infty = 5.8 \times 10^6$ m^{-1}, (*b*) $Re_\infty = 7.6 \times 10^6$ m^{-1}.

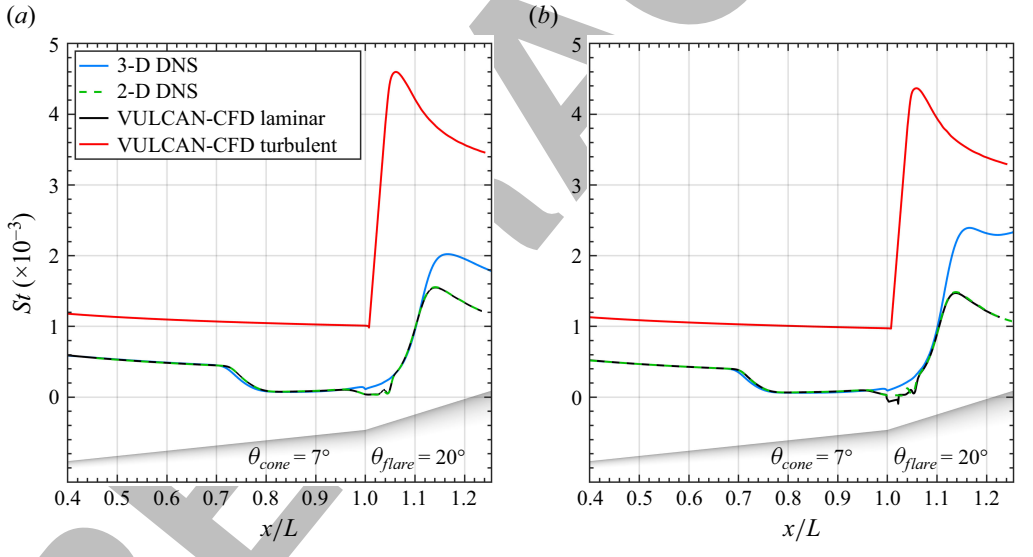


Figure 15. Comparison of base-flow and time-/spanwise-averaged mean-flow solutions ($r_n = 0.99$ mm); (*a*) $Re_\infty = 5.8 \times 10^6$ m^{-1}, (*b*) $Re_\infty = 7.6 \times 10^6$ m^{-1}.

and reattachment by the reverse, from negative to positive. Time averages were computed over snapshots spanning the saturated portion of each case, as given in table 5. For $Re_\infty = 5.8 \times 10^6$ m^{-1}, separation occurs at $x_s/L = 0.735$ while reattachment ranges from $x_r/L = 1.120$ to 1.132 during the saturated regime. At $Re_\infty = 7.6 \times 10^6$ m^{-1}, separation shifts upstream to $x_s/L = 0.711$ while reattachment remains nearly unchanged. The Reynolds-number dependence of x_s and x_r agrees with VULCAN-CFD base-flow results (figure 6). Although the experimental model ends at $x/L = 1.13$, computations extend the domain, capturing the full evolution of the reattached boundary layer.

https://doi.org/10.1017/jfm.2025.10905

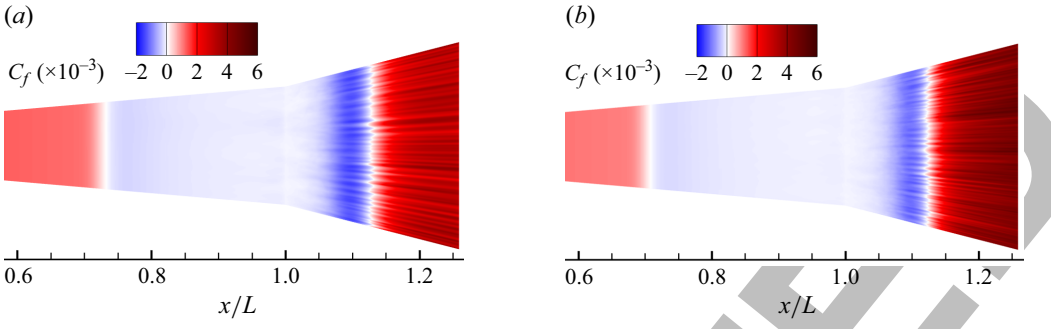


Figure 16. The DNS-computed time-averaged skin-friction contours ($r_n = 0.99$ mm). (*a*) $Re_\infty = 5.8 \times 10^6$ m^{-1}, (*b*) $Re_\infty = 7.6 \times 10^6$ m^{-1}

6. Mean-flow results

The mean flow of the flare-induced SWBLI is analysed to study the stability of the flow prior to the interaction, through the separated shear layer, and downstream of reattachment. By leveraging surface heating and off-wall density data from computational predictions and experimental measurements, the boundary-layer state across the model is assessed for varying Re_∞ and nose tip bluntness. Additionally, trends in separation, reattachment, and transition locations are examined.

6.1. *Global surface heating*

Infrared thermography provided high-spatial-resolution, non-intrusive, quantitative measurements of the surface temperature distribution, from which surface heat flux and Stanton number were calculated. Figure 17 presents global experimental *St* distributions temporally filtered over 0.11 s (40 frames) at $Re_\infty = 7.6 \times 10^6$ and 10.0×10^6 m^{-1} for $r_n = 0.99$ mm. The streamwise and centreline-normal coordinates, x and y, are normalised by the cone length for $r_n = 0.99$ mm ($L = 406.6$ mm) such that the cone–flare junction is located at $x/L = 1$. The distinct decrease in *St* upstream of the cone–flare junction indicates laminar boundary-layer separation. This low-heating region is commonly referred to as a '*St* bucket'. As will be shown in § 6.3, the point at which *St* begins to decrement aligns excellently with separation. The abrupt increase in *St* along the flare correlates closely with the reattachment location.

Streamwise *St* profiles facilitate a more in-depth comparison of separation, reattachment, and the overall state of the flow. Figure 18 presents spanwise-averaged, experimental streamwise *St* profiles for the five primary Re_∞ conditions for $r_n = 0.99$ mm. The profiles on the cone (figure 18*a*) and flare (figure 18*b*) are plotted separately to independently optimise their scales. Time-averaged DNS-computed *St* profiles for $Re_\infty = 5.8 \times 10^6$ and 7.6×10^6 m^{-1} are provided for comparison. Laminar and turbulent VULCAN-CFD computed *St* profiles at the minimum and maximum Re_∞ are also included to assess the boundary-layer state. Off-wall separation and reattachment locations (see § 6.2) are denoted by '○' for experiment, '△' for DNS and '□' for VULCAN-CFD, with colours corresponding to Re_∞. Note that computed reattachment locations for laminar VULCAN-CFD and DNS are outside of the experimental domain (refer to table 6 and figure 12*b*). Turbulent RANS simulations indicate that the SWBLI strength is insufficient to induce flow separation.

On the cone, upstream of the *St* buckets, the experimentally measured and DNS-computed *St* profiles align closely with one another and are within the range of the

RETRACTED

https://doi.org/10.1017/jfm.2025.10905

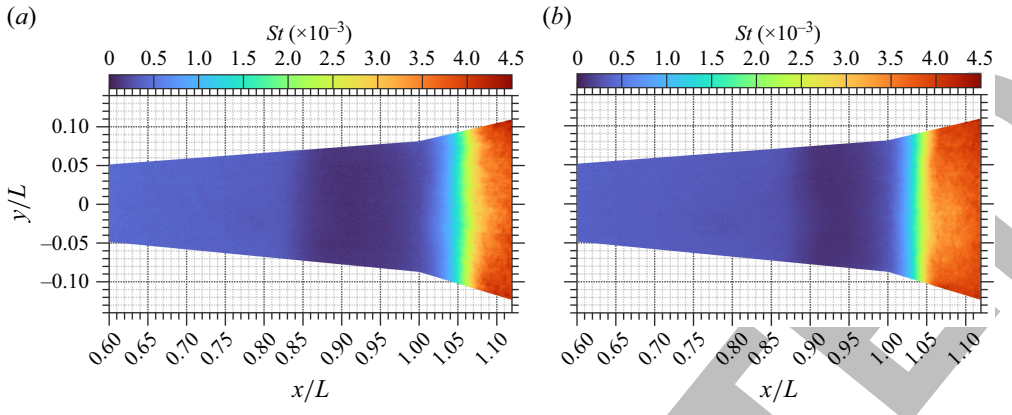


Figure 17. Time-averaged St distributions ($r_n = 0.99$ mm). (*a*) $Re_\infty = 7.6 \times 10^6$ m^{-1}, (*b*) $Re_\infty = 10.0 \times 10^6$ m^{-1}

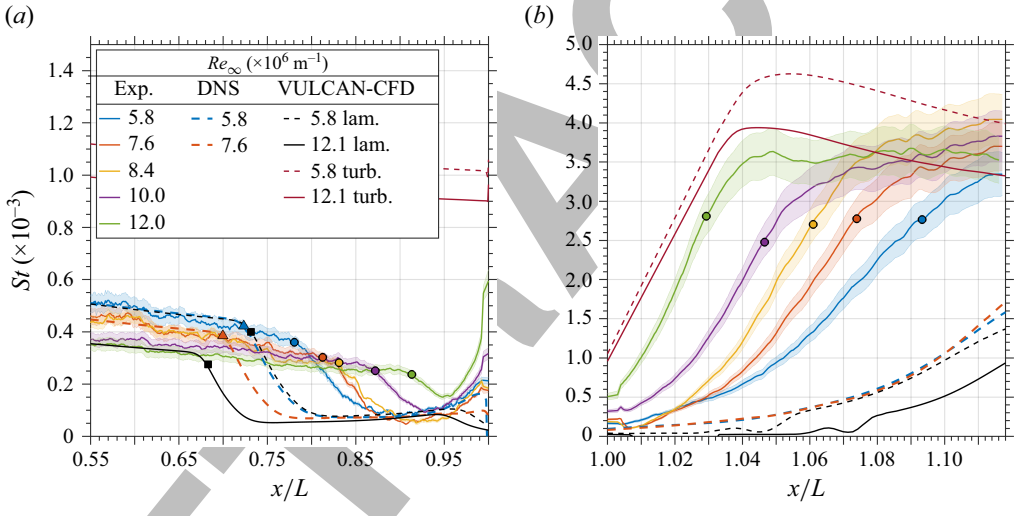


Figure 18. Value of $St(x/L)$ ($r_n = 0.99$ mm). Separation and reattachment locations are denoted by '○' for experiment, '△' for DNS and '□' for VULCAN-CFD. (*a*) Cone, (*b*) Flare.

laminar VULCAN-CFD solutions for the highest and lowest Re_∞. The presence of St buckets, coupled with the strong agreement with the laminar computed solutions, substantiates that the boundary layer remained laminar prior to separation at all Re_∞ for both the experimental and DNS results. For $Re_\infty = 5.8 \times 10^6$ m^{-1}, the DNS predicts separation the earliest, followed by VULCAN-CFD, and the experimental results occur farthest downstream. In the experiment, as Re_∞ increases, the separation location shifts downstream. Davami *et al.* (2025*c*) showed that the angular deflection of the flow at separation is largely insensitive to Re_∞; therefore, as Re_∞ increases, reattachment concomitantly shifts upstream, and the separation bubble shrinks. The trend of a progressively smaller separation bubble with increasing Re_∞ is indicative of a transitional SWBLI, indicating that the flow is transitioning along the shear layer or just downstream of reattachment (Becker 1956; Babinsky & Harvey 2011; Cao *et al.* 2024). The opposite trend is predicted by VULCAN-CFD, as expected, since the flow is entirely laminar throughout

REJECTED

https://doi.org/10.1017/jfm.2025.10905

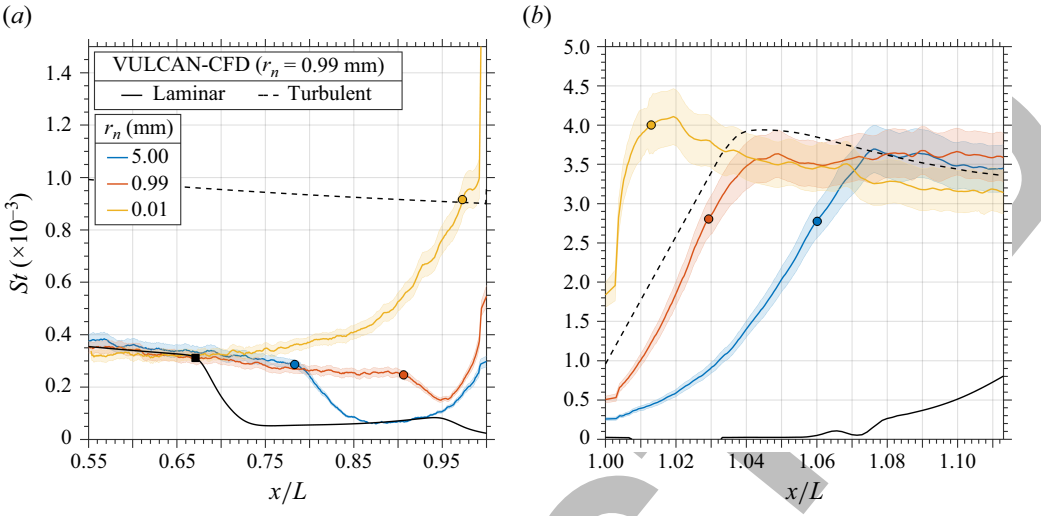


Figure 19. Effect of nose radius on St for $Re_\infty = 12 \times 10^6$ m^{-1}. Markers denote separation and reattachment locations. (*a*) Cone, (*b*) Flare.

the computational domain (i.e. a fully laminar SWBLI). The DNS results predict an upstream shift in separation as Re_∞ increases.

On the flare, the flow state is assessed experimentally by analysing the streamwise behaviour of Stanton number. Davami *et al.* (2025*c*) succinctly summarised that streamwise St can display zero, one or two local maxima, contingent on the flow state on the flare. For all Re_∞ except the highest, St increases consistently until the end of the flare, with no discernible maxima. This lack of a peak suggests either a transitional reattaching boundary layer or the absence of reattachment. However, since off-wall measurements confirm reattachment, it indicates that a transitional boundary layer reattaches. This is corroborated by the experimental St being between the laminar and turbulent values computed by VULCAN-CFD. For the highest Re_∞, the heating profile exhibits two peaks. The first peak, caused by compression, suggests that the boundary layer is likely turbulent at reattachment, especially since the heating magnitude closely matches the corresponding RANS computation. The second peak occurs farther downstream of reattachment at $x/L = 1.09$, and is due to separation happening close to (but upstream of) the corner, where the separation and reattachment shocks interact (Running *et al.* 2019). This interaction, an Edney type VI (Edney 1968), generates an expansion wave that impinges on the flare downstream of reattachment, reducing both density and heating. Discrepancies in reattachment heating and topological differences of the SWBLI between experiment and computation are discussed and analysed in § 6.4.

Nose radius affected the SWBLI through the modulated flow on the conical forebody. Figure 19 presents $St(x/L)$ for $Re_\infty = 12.0 \times 10^6$ m^{-1} and nose radii of 5.00, 0.99 and 0.01 mm, along with laminar and turbulent VULCAN–CFD St profiles for $r_n = 0.99$ mm. The flow separated earliest for the 5.00 mm radius nose, thus delaying reattachment. This behaviour was consistent across all Re_∞, as higher nose bluntness stabilises the flow on the conical forebody (Brinich 1957). Bibin *et al.* (2016) showed numerically that while leading-edge bluntness reduces separation in 2-D SWBLIs by producing a thicker entropy layer and stronger favourable pressure gradient, in axisymmetric flows the thinner entropy layer resulting from 3-D relieving effects increases separation length.

https://doi.org/10.1017/jfm.2025.10905

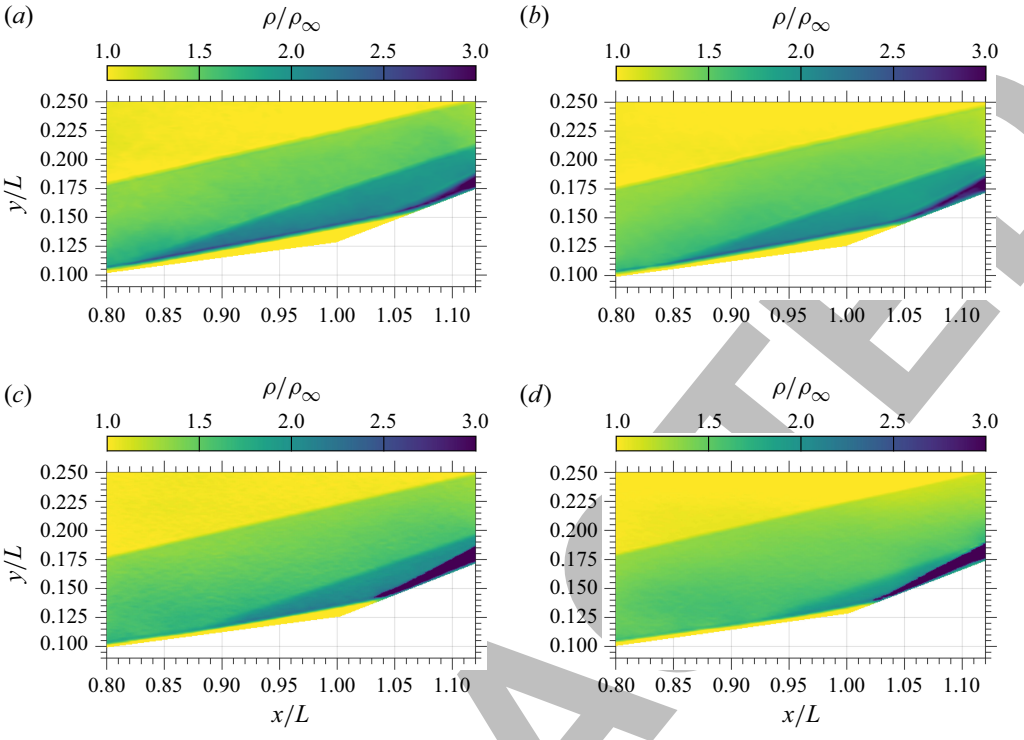


Figure 20. Experimental density fields ($r_n = 0.99$ mm); (*a*) $Re_\infty = 5.8 \times 10^6$ m^{-1}, (*b*) $Re_\infty = 7.6 \times 10^6$ m^{-1}, (*c*) $Re_\infty = 10.0 \times 10^6$ m^{-1}, (*d*) $Re_\infty = 12.0 \times 10^6$ m^{-1}.

For all nose radii in figure 19, surface heating and off-wall measurements indicate laminar flow at separation and transitional flow at reattachment. For the sharp nose, *St* rises upstream of the cone–flare junction, and since it remains below the turbulent computation, the boundary layer is inferred to be transitioning prior to the SWBLI. The stability analysis shows that the *N*-factor exceeds 8 at the cone–flare junction for $Re_\infty = 12.1 \times 10^6$ m^{-1} (figure 8*b*), above critical levels ($N \approx 7$) typically associated with transition onset in conventional hypersonic facilities (Horvath *et al.* 2002). For the sharp nose tip at $Re_\infty = 12.0 \times 10^6$ m^{-1}, the BOS-identified separation location coincides with the streamwise *St* plateau at $x/L = 0.98$. A slight plateau followed by an abrupt *St* increase is therefore taken as the surface-heating signature of transitional separation. A distinct heating peak at reattachment indicates that the flow is nearing the end of transition, as further supported by the close agreement with the turbulent RANS VULCAN–CFD heating magnitude.

6.2. *Global off-wall density*

Concurrent with IR thermography, BOS measured off-wall density and density-gradient fields provided high-spatial-resolution, non-intrusive, quantitative assessment of separation and reattachment locations (Davami *et al.* 2025*b*,*c*). Figure 20 shows normalised density fields for $Re_\infty = 5.8 \times 10^6$ m^{-1} to 12.0×10^6 m^{-1} for $r_n = 0.99$ mm (see table 1). At each Re_∞, the bow shock enters at $y/L = 0.175$, with $\rho/\rho_\infty > 1$ downstream. The separation shock is indicated by a rapid near-surface density rise ($\rho/\rho_\infty \approx 2.0$), while the reattachment shock occurs near the flare surface ($\rho/\rho_\infty \approx 3.0$), enclosing a low-density recirculation bubble. As Re_∞ increases, the boundary layer on the

RETRACTED

https://doi.org/10.1017/jfm.2025.10905

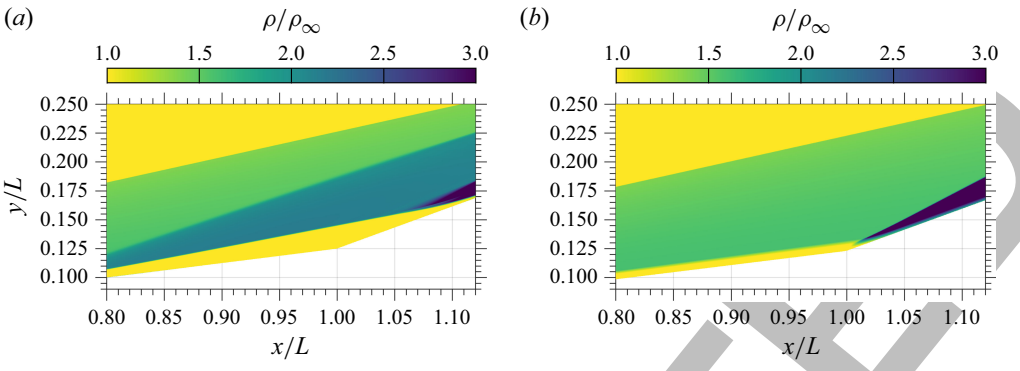


Figure 21. VULCAN-CFD density fields ($r_n = 0.99$ mm). (*a*) Laminar, $Re_\infty = 5.8 \times 10^6$ m^{-1}. (*b*) Turbulent (RANS), $Re_\infty = 12.1 \times 10^6$ m^{-1}.

conical forebody thins, bringing the shear layer closer to the surface, while the separation point shifts downstream, the reattachment point moves upstream, and the recirculation bubble shrinks, consistent with IR results.

Figure 21 presents normalised density fields computed from VULCAN-CFD for $r_n = 0.99$ mm; figure 21(*a*) is a laminar base flow at $Re_\infty = 5.8 \times 10^6$ m^{-1} and figure 21(*b*) is a turbulent RANS solution at $Re_\infty = 12.1 \times 10^6$ m^{-1}. For $Re_\infty = 5.8 \times 10^6$ m^{-1}, the computed and experimental density fields agree excellently. Although the separation and reattachment locations differ slightly – because the experimental SWBLI is transitional, whereas the computation is fully laminar – the density magnitudes match well throughout the domain except very near the wall, due to unknown boundary conditions along the surface (Liu & Katz 2006; Liu & Moreto 2021; Abassi, Wang & Liu 2025).

As was discussed in § 6.1, for a fully laminar SWBLI, the separation bubble increases in size as Re_∞ increases. Consequently, comparisons between laminar base flows and experimental density fields at higher Re_∞ demonstrate worse agreement regarding separation. The turbulent VULCAN-CFD results reveal that, regardless of Re_∞, the adverse pressure gradient is insufficient to cause separation and the normalised density fields are virtually identical. As Re_∞ increases in the experiment, the transition front shifts upstream of the cone–flare junction. Thus, the experimental density field progressively approaches the fully turbulent VULCAN-CFD solution.

6.3. *Global comparison of surface and off-wall results*

Surface and off-wall results are presented in figure 22, for time-averaged experimental measurements, laminar VULCAN-CFD base flow and DNS time averaged over the linear and saturated growth regimes, for $Re_\infty = 5.8 \times 10^6$ m^{-1} and $r_n = 0.99$ mm. Stanton number distributions are the centre contour, with normalised density shown above and density-gradient magnitude below. The experimental peak *St* exceeds the DNS predictions by more than a factor of two (note the different scales for the *St* contours). The discrepancies in flare heating are expected to be due to fundamental differences in disturbance environments between experiments and simulations. This is consistent with previous SWBLI experiments, which show that reattachment heating under noisy conditions can exceed that in quiet flow by more than a factor of two (Schneider 2004; Simeonides 2008; Chynoweth *et al.* 2017; Benitez *et al.* 2021; Leidy *et al.* 2025). Discrepancies in separation length between experiment and simulation are also evident. Previous studies have demonstrated that free-stream noise strongly influences the

RETRACTED

https://doi.org/10.1017/jfm.2025.10905

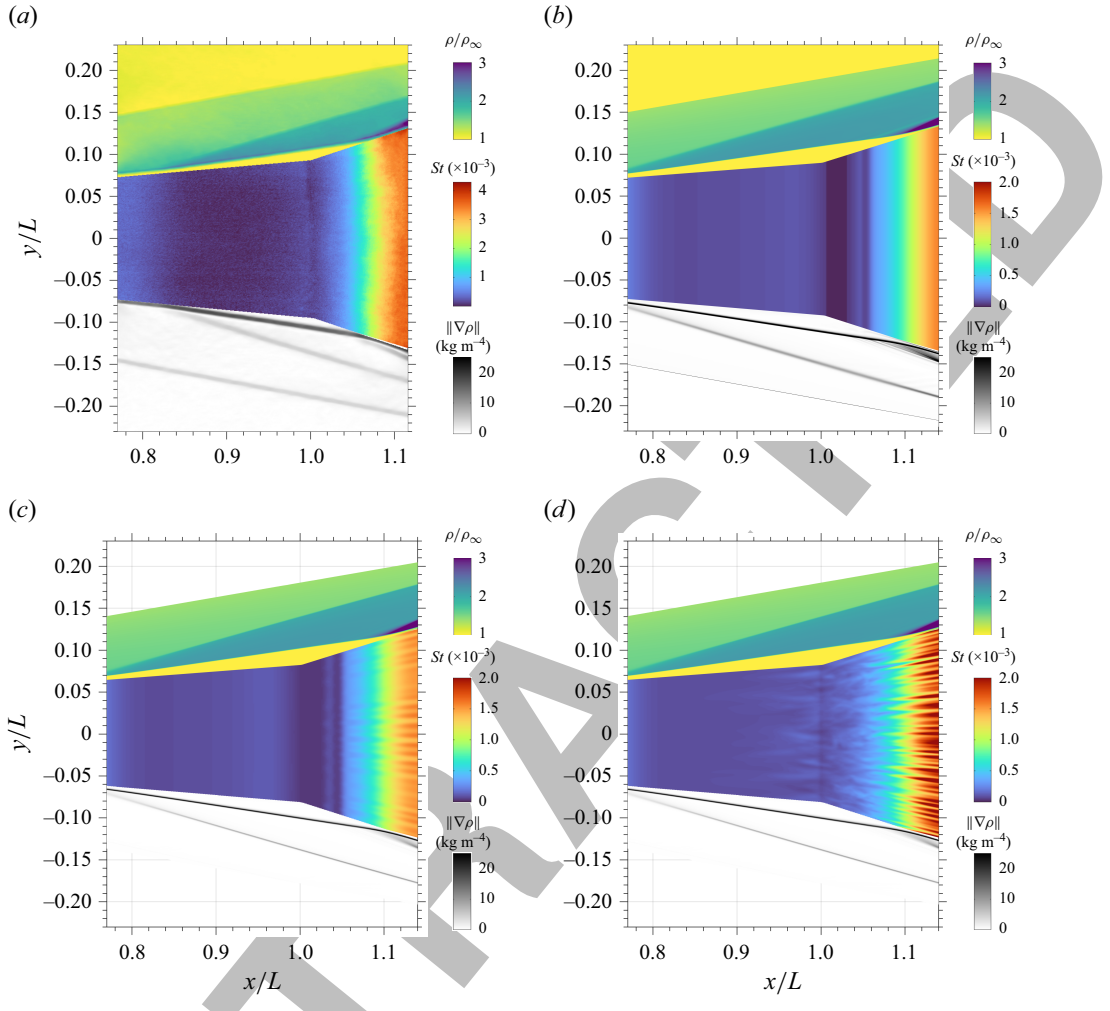


Figure 22. Surface and off-wall results ($Re_\infty = 5.8 \times 10^6$ m^{-1} and $r_n = 0.99$ mm). (*a*) Experiment, (*b*) laminar base flow, (*c*) DNS (linear growth regime), (*d*) DNS (saturated growth regime).

separation and reattachment locations for transitional flare-induced SWBLIs (Threadgill *et al.* 2024; Davami *et al.* 2025*c*; Leidy *et al.* 2025).

Comparison of the global off-wall and surface results in figure 22 reveals good agreement between the separation shock foot location and the decrease in St on the conical forebody. At reattachment, the shock foot impinges upstream of peak St, with the maximum heating rates observed near the end of the flare. Thermal streaks are present on the flare, extending from within the separation bubble downstream to the reattachment shock and continuing to the end of the flare in both experiment and DNS.

Measured and computed normalised separation length l/L (where $l \equiv x_r - x_s$) are shown in figure 23(*a*) as functions of Re_∞ for all nose radii. Experimentally, a separation bubble was present for all Re_∞, with its mean length decreasing as Re_∞ increased due to the downstream shift of the separation point. This trend indicated a transitional interaction, where the flow was laminar before separation and became transitional or turbulent upon reattachment at higher Re_∞. In contrast, the VULCAN-CFD computations were run with a

RETRACTED

https://doi.org/10.1017/jfm.2025.10905

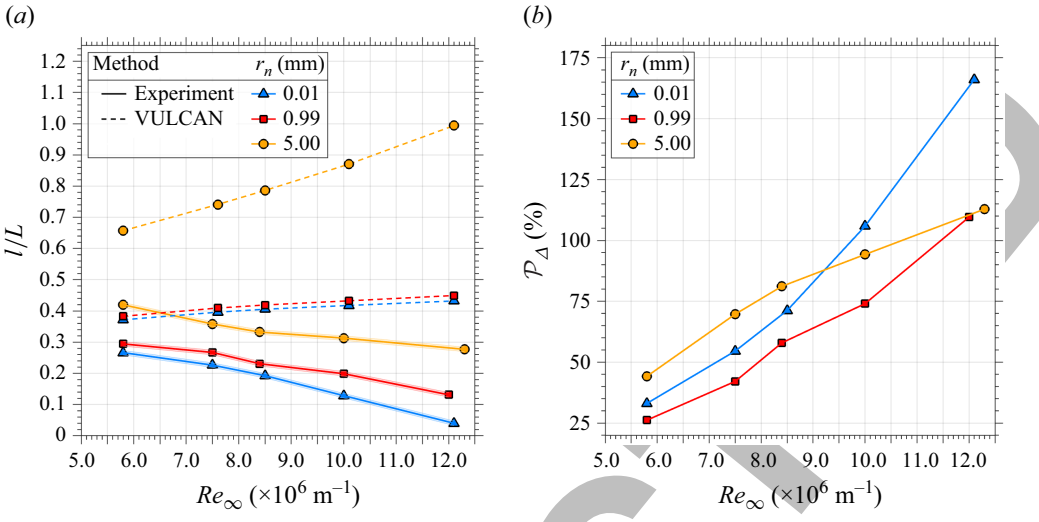


Figure 23. Measured and computed separation bubble comparison. (*a*) Separation length. (*b*) Per cent difference.

fully laminar separation bubble, leading to an increase in separation length with increasing Re_∞ as well as a larger separated region for a given Re_∞ compared with the experiment. For both the experiment and computations, a blunter nose results in a larger separation bubble. Figure 23(*b*) presents the per cent difference between measured and computed separation lengths as a function of Re_∞ for each nose radius.

Davami *et al.* (2025*c*) compared flight test data from the ROcket Technology Experiment on Transition (ROTEX-T) cone–flare vehicle with experiments from multiple conventional hypersonic facilities and computations using various computational fluid dynamics (CFD) codes. When the Reynolds number based on cone length was matched, both ground tests and flight exhibited consistent trends: increasing Reynolds number shifted the separation and reattachment points toward the cone–flare junction, shortening the separation region. Heating profiles also followed the experimental trends shown in figure 18. Leidy *et al.* (2025) and Davami *et al.* (2025*d*) investigated ROTEX-T under quiet-flow conditions and observed similar trends. For N-factors below the onset of transition, the separation bubble closely matches the laminar base flow predicted by computations. At the onset of transition, the experimentally measured topology of the SWBLI diverges appreciably from the computed laminar base flow.

The sensitivity of the mean flow – observed across quiet and noisy experimental facilities as well as in flight – results in substantial discrepancies between experimental observations and computational predictions. This emphasises the critical need for transitional SWBLI simulation models that extend beyond replicating fully laminar or turbulent states to accurately capture the intermediate transitional stages. These limitations in current computational approaches directly impact design and control strategies for high-speed vehicles equipped with control surfaces (Maughmer, Long & Pagano 1992; Berry *et al.* 2001; Horvath *et al.* 2004; Bur & Chanetz 2009; Coleman & Faruqi 2009; Lee *et al.* 2024).

6.4. *Effect of inflow forcing*

The experiments analysed in this work were conducted under conventional-noise conditions, with elevated free-stream noise introducing inflow and free-stream forcing.

https://doi.org/10.1017/jfm.2025.10905

In contrast, the DNS were performed without external disturbances at the inflow or in the free stream, with instabilities developing solely from minimal numerical round-off perturbations. To examine the observed differences in heating rates along the flare and separation bubble topology, additional numerical simulations with inflow forcing disturbances were performed.

Here, we use the broadband inflow forcing approach by Cao *et al.* (2024) as a simple model to trigger convective instabilities in the laminar boundary layer, which (at least qualitatively) accounts for the effect of ambient disturbances in the experiment. The induced disturbances have been shown to have a broadband spectrum in both frequency and wavelength and therefore allow 'naturally' selected preferred modes (Cao *et al.* 2024). The method uses the FORTRAN pseudo-random number generator to impose random spanwise-velocity perturbation (w') into the flow at a user-specified domain as

$$w'_{i,j,k,n}/U_\infty = A(2r-1), \tag{6.1}$$

where $r =$ random_number(), i, j and k are the grid points in the streamwise, azimuthal and wall-normal directions, respectively, n represents the time step and A is the specified amplitude of the perturbations and is referred to in percentage of the free-stream velocity U_∞ in this paper. For the results presented here, spanwise-velocity disturbances are applied over a singular streamwise plane of $i = 6$ (which is 6 grid points downstream from the inlet), and the perturbation is updated every 50 time steps to ensure a sufficient time for the convection of disturbances through grid points. The amplitude A is systematically altered from 0.625 % and 5 % to show the effect of forcing amplitude on boundary-layer instability growth A_w (5.8) and surface heating St. The simulations were performed using the same grid resolution as in the baseline case, but with a narrower span of $\phi = 7.2°$ (corresponding to $m = 50$), thus $N_x \times N_\phi \times N_r = 740 \times 64 \times 540$.

Figures 24 and 25 present A_w and St as a function of inflow forcing amplitude A at $Re_\infty = 5.8 \times 10^6$ and 7.6×10^6 m^{-1}, respectively. As expected, the addition of inflow forcing reduces the time it takes for boundary-layer instabilities to become saturated. However, the linear growth rate and post-saturation disturbance amplitude remain the same as in the zero-forcing case. These results show that by varying the amplitude of the broadband inflow forcing from 0.625 % to 5 % significantly increases the peak heating rate in the post-reattachment region, leading to a closer match with the experimental data. The DNS results reproduce experimental flare-heating trends, demonstrating that reattachment heating on the flare is highly sensitive to inflow disturbances. Accounting for inflow forcing in the simulations shows that inflow disturbance spectra directly determine the thermal loads, explaining the persistently elevated heating rates observed in prior studies under noisy flow conditions compared with quiet environments.

Note that for the non-zero-forcing cases, the overall characteristics of the laminar separation bubble such as the bubble size and the locations of separation and reattachment remain similar to those of the zero-forcing case. Previous studies have demonstrated that axisymmetric transitional separation bubbles contract with increasing Re and that free-stream noise further contracts the bubble for a given Re compared with quiet environments (Leidy *et al.* 2025). Tsakagiannis *et al.* (2025*a*) captured this effect in DNS by performing a suite of controlled forcing simulations. By progressively increasing the amplitude of forcing on the dominant convective instability upstream of separation, the bubble eventually contracts in length. The different bubble behaviours suggest the importance of forcing characteristics in bubble topology. Another possible factor in the incomplete agreement between DNS and experiment is that the as-computed flare was extended to

RETRACTED

https://doi.org/10.1017/jfm.2025.10905

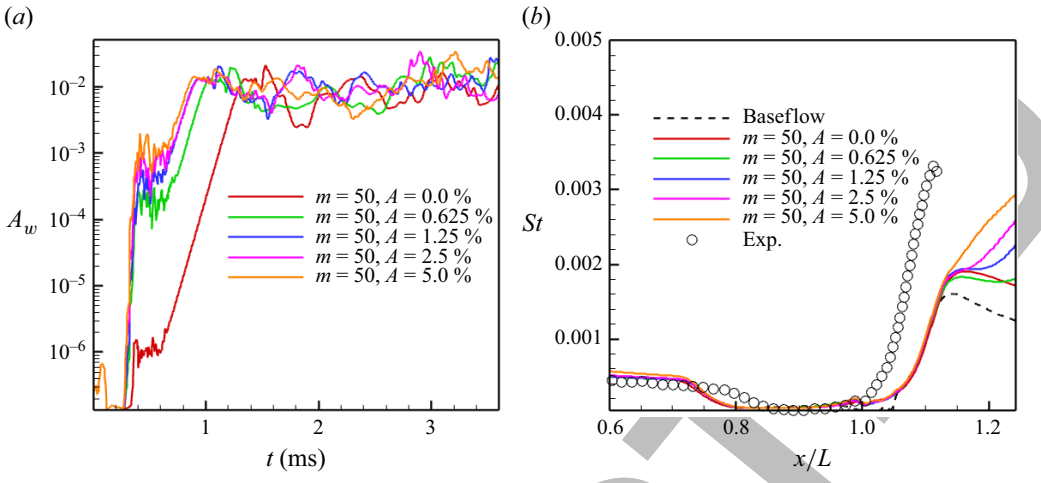


Figure 24. Effect of inflow forcing on DNS for $Re_\infty = 5.8 \times 10^6$ m^{-1} with $r_n = 0.99$ mm; (*a*) A_w near reattachment ($x/L = 1.05$)., (*b*) *St*.

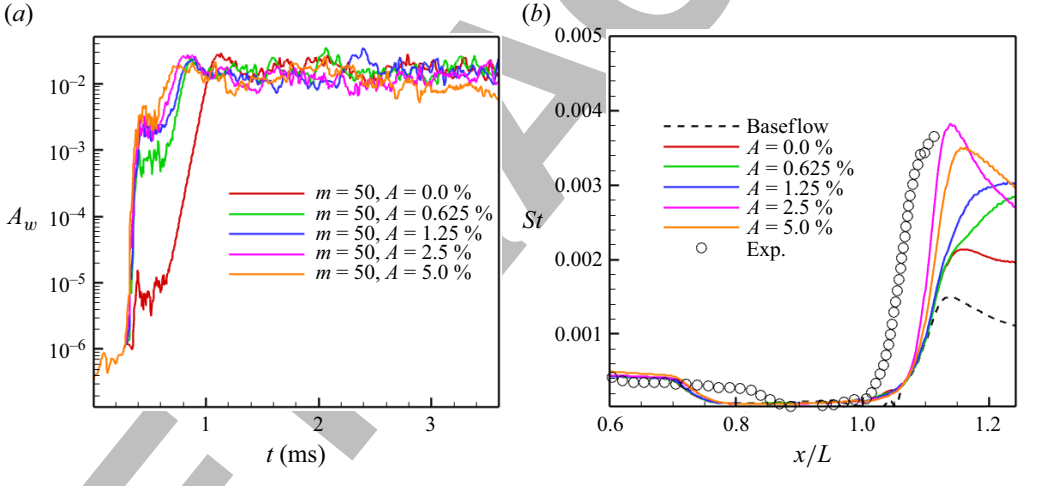


Figure 25. Effect of inflow forcing on DNS for $Re_\infty = 7.6 \times 10^6$ m^{-1} with $r_n = 0.99$ mm; (*a*) A_w near reattachment ($x/L = 1.05$), (*b*) *St*.

reduce the influence of the base wake on reattachment (Davami *et al.* 2025*d*; Leidy *et al.* 2025).

7. Unsteady results

Global stability analysis shows the flow is globally unstable to stationary 3-D disturbances concentrated in the recirculation bubble. However, it remains to be shown that this instability drives the formation of the experimentally observed streaks near reattachment, which could be dominated by alternative mechanisms, such as Görtler or convective instabilities. To make this determination, a three-way comparison was made of the dominant azimuthal wavenumbers as computed by GSA and DNS, and measured experimentally.

https://doi.org/10.1017/jfm.2025.10905

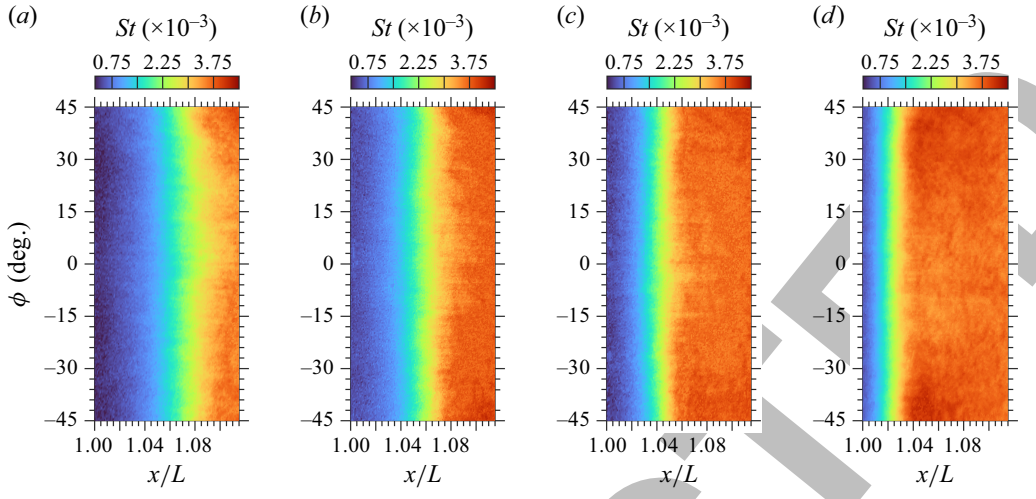


Figure 26. Experimental *St* distributions on the flare ($r_n = 0.99$ mm); (*a*) 5.8×10^6 m^{-1}, (*b*) 7.5×10^6 m^{-1}, (*c*) 10.0×10^6 m^{-1}, (*d*) 12.0×10^6 m^{-1}.

7.1. *Streak instability*

Streamwise striations were experimentally observed on the flare for all Re_∞, indicating the presence of azimuthally periodic perturbations. Figure 26 presents instantaneous *St* distributions, with the non-dimensionalised streamwise coordinate on the abscissa and the azimuthal angle (ϕ) on the ordinate. Transitional separation bubbles are highly sensitive to angle of attack (Davami *et al.* 2023*b*); even 0.15° can cause significant changes in spanwise heating at reattachment (Benitez *et al.* 2021; Leidy *et al.* 2025). The spanwise variation in *St* is minimal for all Re_∞ in figure 26, indicating that the model was well aligned with respect to the free stream. For the cone–flare configuration, the streaks have smaller wavelengths and amplitudes than 2-D SWBLIs (Running *et al.* 2020). Particularly for small turning angles ($\lesssim 15°$) and depending on the nose radius, the streaks may not be detectable by thermography due to a low signal-to-noise ratio (Benitez *et al.* 2024*a*; Leidy *et al.* 2025). Although lateral heat conduction may contribute to slight attenuation of the thermal striations, its influence is limited due to the short test durations (Running *et al.* 2020). The streaks wavelength decreases as Re_∞ increases, which is consistent with the GSA and DNS. The amplitude and downstream extent of the streaks also decrease as Re_∞ increases because of the accelerated transition to turbulence. Recall that at $Re_\infty = 12.0 \times 10^6$ m^{-1}, the flow was nearly turbulent at reattachment.

As a starting point, the case with $Re_\infty = 5.8 \times 10^6$ m^{-1} and $r_n = 0.99$ mm is examined for comparisons between experiment, DNS and GSA. This case exhibits the closest mean-flow agreement between experiment and computations among all conditions tested, with the separation bubble length differing by 26 % (recall figure 23*b*). Quiet-flow experiments on this configuration indicated that, despite reattachment occurring approximately 23 % closer to the cone–flare junction than predicted by laminar base flows, the dominant instability frequencies and mode shapes matched closely provided that nonlinear activity at reattachment was not excessive (i.e. triadic interactions were confined to relatively low frequencies) (Davami *et al.* 2025*d*).

Figure 27 presents the corresponding heat streaks along the flare for experiment and time-averaged DNS for the linear and saturated growth regimes. For improved visualisation (here only), the streaks are enhanced by subtracting the *St* distribution from

REJECTED

https://doi.org/10.1017/jfm.2025.10905

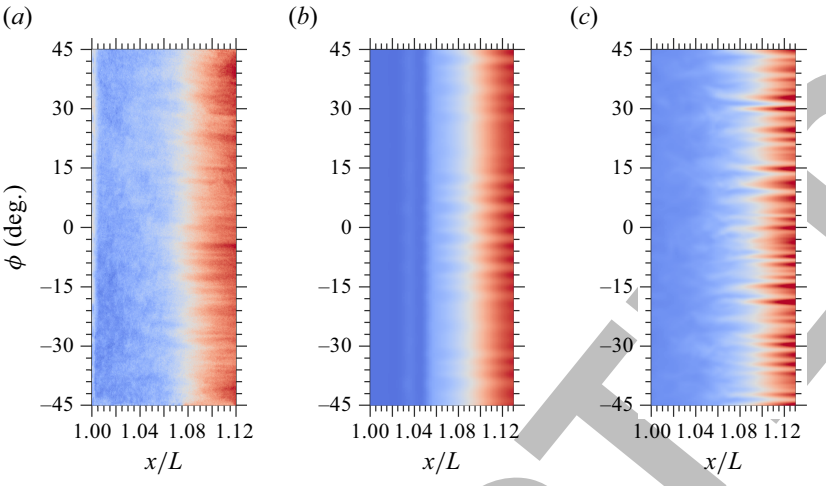


Figure 27. Thermal streaks ($Re_\infty = 5.8 \times 10^6$ m^{-1} and $r_n = 0.99$ mm). (*a*) Experiment, (*b*) DNS (linear), (*c*) DNS (saturated).

an earlier steady-flow period, with contour levels adjusted to increase their visibility. As the DNS simulation evolves from the linear growth phase to saturation, global unstable modes induce spanwise modulation near reattachment, causing the flow to break down from axisymmetric to three-dimensional on the flare.

The streaks are initially characterised by quantifying the time-varying azimuthal wavenumber spectrum locally. Discrete Fourier transforms (DFTs) of *St* along the azimuth locations were computed, yielding amplitudes as functions of wavenumber. The input to the DFT was detrended *St* profiles extracted along $\phi = [-45°, 45°]$ and averaged in the streamwise direction over approximately 2 mm. For the experiment, this was performed without temporal averaging for each of 150 snapshots, a 0.42 s duration. The uncertainty quantification in wavenumber followed Running *et al.* (2020). For the DNS, the linear (300 snapshots, 0.27 ms) and saturated (4392 snapshots, 4.8 ms) growth regimes were analysed separately. The DFTs were calculated upstream and downstream of reattachment to investigate the evolution of streaks through the strong compression at reattachment.

Spectral maps of azimuthal wavenumber m at $Re_\infty = 5.8 \times 10^6$ m^{-1} with $r_n = 0.99$ mm are shown upstream (figure 28) and downstream (figure 29) of reattachment. Below each spectral map, the time-averaged amplitude is plotted as a function of the azimuthal wavenumber. For this case, GSA showed that the stationary global mode with $m = 50$ exhibited the largest growth rate. The locations analysed for the experiment are shifted upstream to maintain the same relative distance from reattachment as in the computations.

Upstream of reattachment, the experiment displays a broad wavenumber spectrum spanning $m = 30$–130, with a time-averaged dominant wavenumber of $m = 50 \pm 3$ (figure 28*a*). The DNS confirms the dominance of $m = 50$ during the linear growth period (figure 28*b*). The stationary global mode is markedly more energetic than the oscillatory modes identified by GSA, which reflects its large exponential growth rate. During the saturated regime, energy spreads across a wider wavenumber range with $m = 50$ being most energetic on average, consistent with the experiment (figure 28*c*).

Downstream of reattachment, the experiment reveals two distinct steady wavenumbers: $m = 50 \pm 3$ and its harmonic $m = 100 \pm 3$ (figure 29*a*). In the DNS, the stationary global mode continues to dominate during linear growth (figure 29*b*), even with the local analysis

RETRACTED

https://doi.org/10.1017/jfm.2025.10905

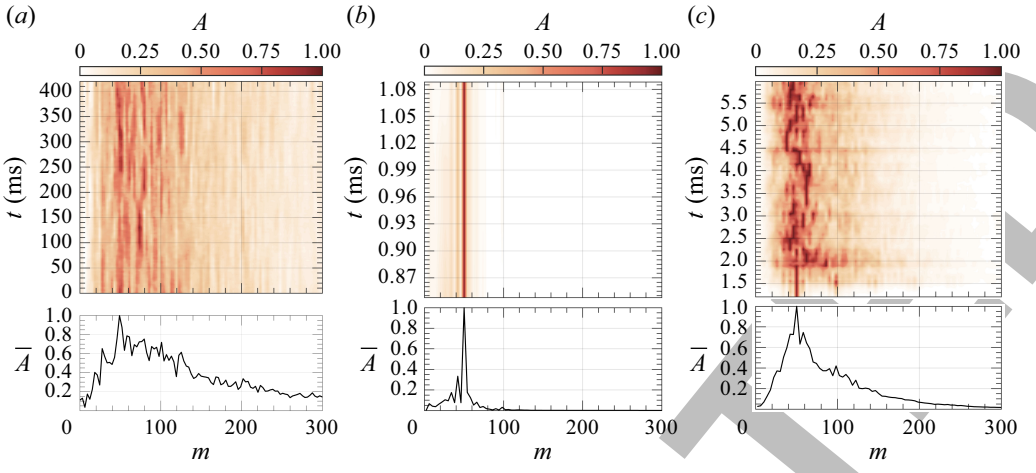


Figure 28. Normalised spectral maps of azimuthal wavenumber (top) and amplitudes (bottom) upstream of reattachment; $Re_\infty = 5.8 \times 10^6$ m^{-1} and $r_n = 0.99$ mm. (*a*) Experiment ($x/L = 1.04$), (*b*) DNS linear ($x/L = 1.05$), (*c*) DNS saturated ($x/L = 1.05$).

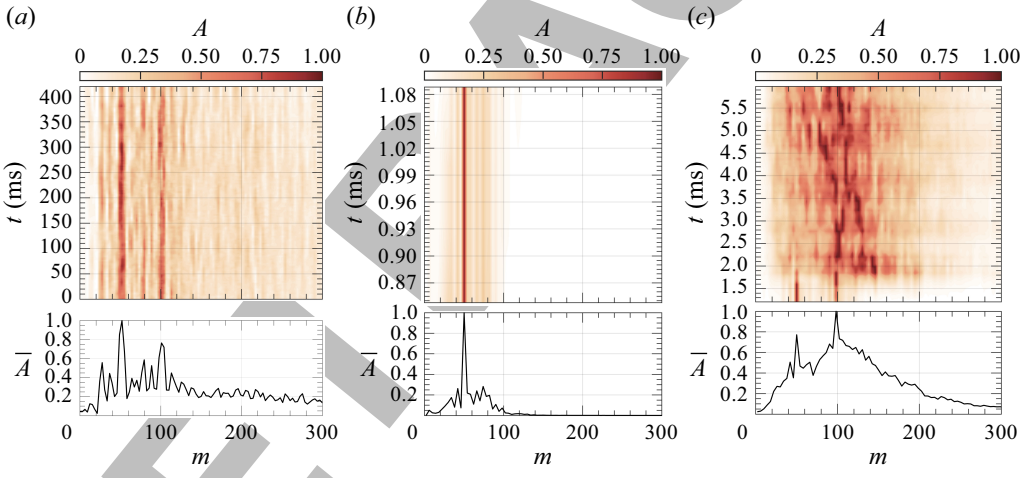


Figure 29. Normalised spectral maps of azimuthal wavenumber (top) and amplitudes (bottom) downstream of reattachment; $Re_\infty = 5.8 \times 10^6$ m^{-1} and $r_n = 0.99$ mm. (*a*) Experiment ($x/L = 1.11$), (*b*) DNS linear ($x/L = 1.15$), (*c*) DNS saturated ($x/L = 1.15$).

being conducted 41 mm downstream of its central location. As the flow in the DNS approaches saturation (figure 29*c*), nonlinear interactions redistribute energy from the dominant wavenumber to its harmonic ($m = 100$) between $t = 1.2$ and 1.5 ms. Nonlinear saturation of the global modes distributes energy across the spectrum $m = 30$–150, with the time-averaged dominant wavenumber corresponding to both the fundamental and its harmonic, as observed in the experiment. The DNS, however, indicates that this far downstream of the global mode, the harmonic gradually begins to dominate over the fundamental. Although other wavenumbers exhibit some content in the experiment and saturated regime of the DNS, none are as dominant or persistent as the primary wavenumber of $m = 50$ or its harmonic.

REJECTED

https://doi.org/10.1017/jfm.2025.10905

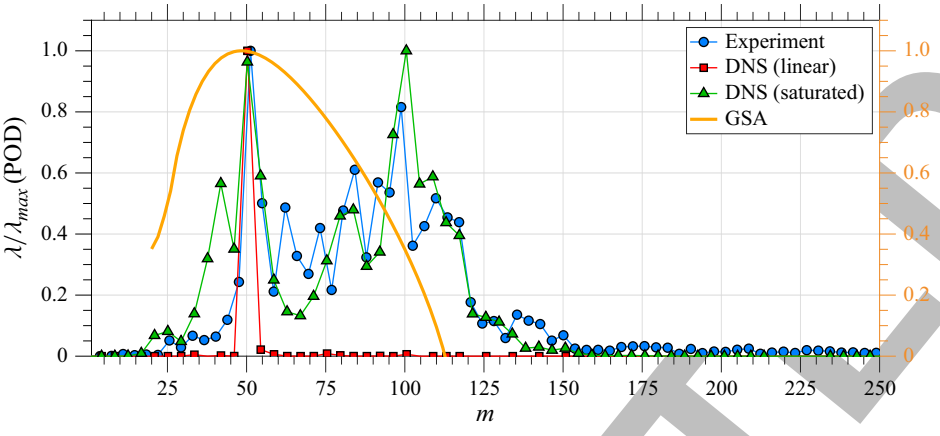


Figure 30. Spectra of normalised POD energy from experiment and DNS and normalised growth rate from GSA ($Re_\infty = 5.8 \times 10^6$ m^{-1} and $r_n = 0.99$ mm).

To better understand the streamwise evolution of streaks originating from the stationary global unstable mode, the thermal striations on the flare were also characterised globally using Fourier decomposition coupled with proper orthogonal decomposition (POD), similar to the analysis by Lugrin, Beneddine & Garnier (2021). The decomposition distinguishes correlated physical information from uncorrelated noise while capturing both spatial and temporal variations in wavenumber. Its input is the entire streamwise extent of the flare, unlike the spectral map analysis, which focused on a specific streamwise location. An azimuthally reconstructed mode shape of a wavenumber thereby highlights where that wavenumber is dominant. At each streamwise station, a DFT of detrended spanwise Stanton number was computed. For the experimental measurements, this was performed for approximately 105 frames, covering 0.3 s, and combined into a matrix of DFT amplitudes as functions of time, wavenumber, and the streamwise spatial coordinate. The POD of this matrix obtains modes for a given wavenumber. Since the decomposition is performed on the DFT output, the energy of a wavenumber is indicated by its highest-energy POD mode.

Figure 30 presents the POD energy (λ) spectrum with a wavenumber resolution of 4. Each spectrum is normalised by its maximum energy to highlight the most dominant wavenumbers. For comparison, the growth rate (σ) spectrum from GSA is also included and normalised the same way. The most energetic wavenumbers correspond closely to those previously identified in the spectral maps downstream of reattachment (figure 29) for both the experiment and DNS. The GSA-predicted dominant wavenumber ($m = 50$) aligns with the highest energy content in the linear growth regime of the DNS. The experiment and saturated DNS match closely: the fundamental and first harmonic dominate the flow globally, while other wavenumbers are moderately amplified. The greater energy at wavenumbers away from the fundamental in the saturated than linear DNS results suggests that saturation of the global modes drives much of the streak amplification. In the experiment, some energy may also arise from convective mechanisms, but under these conditions most of the streak amplification appears to result from global instabilities.

Figure 31 presents the azimuthally reconstructed $m = 50$ mode shape for $Re_\infty = 5.8 \times 10^6$ m^{-1} and $r_n = 0.99$ mm. From GSA, the mode shape is represented by the azimuthally reconstructed real part of the streamwise heat-flux perturbation of the leading stationary disturbance (figure 31*b*) provides the azimuthally reconstructed real part of the streamwise heat-flux perturbation of the leading stationary disturbance

RETRACTED

https://doi.org/10.1017/jfm.2025.10905

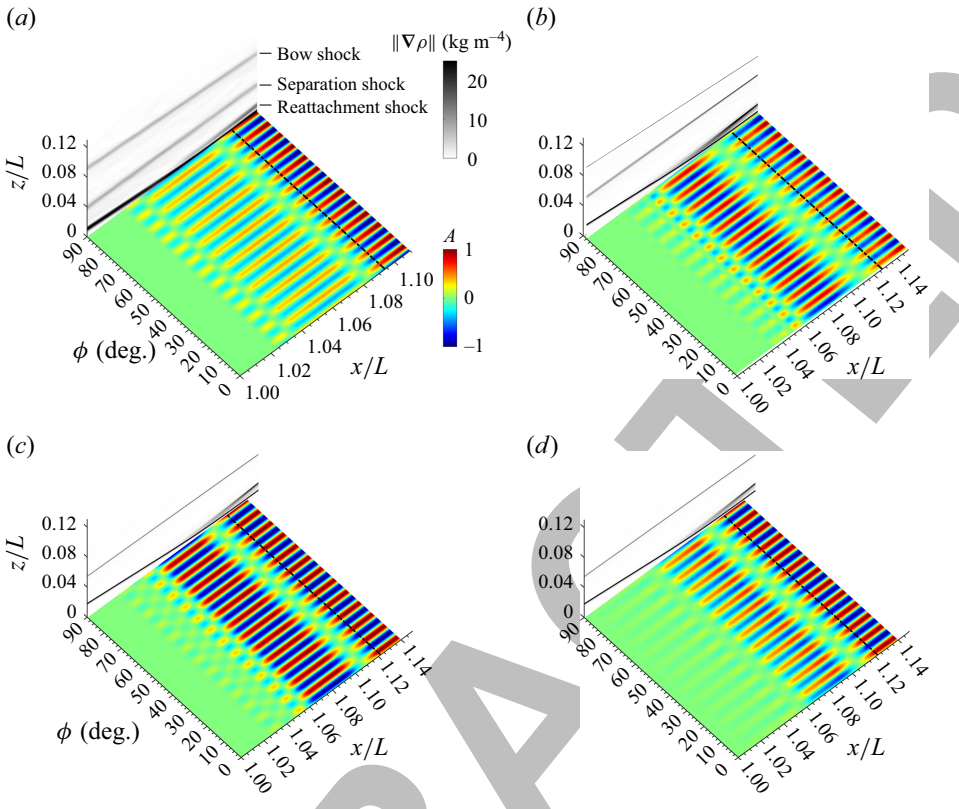


Figure 31. Value of $||\nabla\rho||$ and surface-heating mode shape. Here, $m = 50$, $Re_\infty = 5.8 \times 10^6$ m^{-1} and $r_n = 0.99$ mm. (*a*) Experiment, (*b*) GSA and VULCAN-CFD, (*c*) DNS (linear), (*d*) DNS (saturated).

computed by GSA for the same condition. For each, a dashed black line marks the mean reattachment location. The mode shapes from the experiment, GSA and DNS are similar, each exhibiting neutral lines both upstream of and at reattachment, across which the heat-flux oscillations change sign. The first band of elevated amplitude is of much shorter streamwise extent than the second. The third (post-reattachment) band reaches peak amplitude only at the downstream end of the flare; a longer flare may experience continued amplification.

The magnitude of the density gradient is shown along the x–z plane in figure 31 to provide off-wall context – these streaks originate within the recirculation bubble and amplify downstream of the reattachment shock. Recall the GSA-computed off-wall mode shape for this case was presented in figure 11(*a*), which showed its centre is at $x/L = 1.05$–1.06, matching the neutral line in the mode shape. That the neutral line is observed in the experimentally measured mode shape at $x/L = 1.035$ may suggest that the global instability is centred there – farther upstream than GSA predictions due to the smaller separation bubble in the experiment.

Like the present GSA and DNS, the high-fidelity computational studies of Hildebrand *et al.* (2018), Sidharth & Candler (2018) and Lugrin *et al.* (2022*a*), show that global unstable modes in high-speed recirculation bubbles induce sign changes in the streamwise heat-flux instability modes. The good agreement between the mode shapes, along with the similarity in the most amplified wavenumbers predicted by GSA and DNS, provides

RETRACTED

https://doi.org/10.1017/jfm.2025.10905

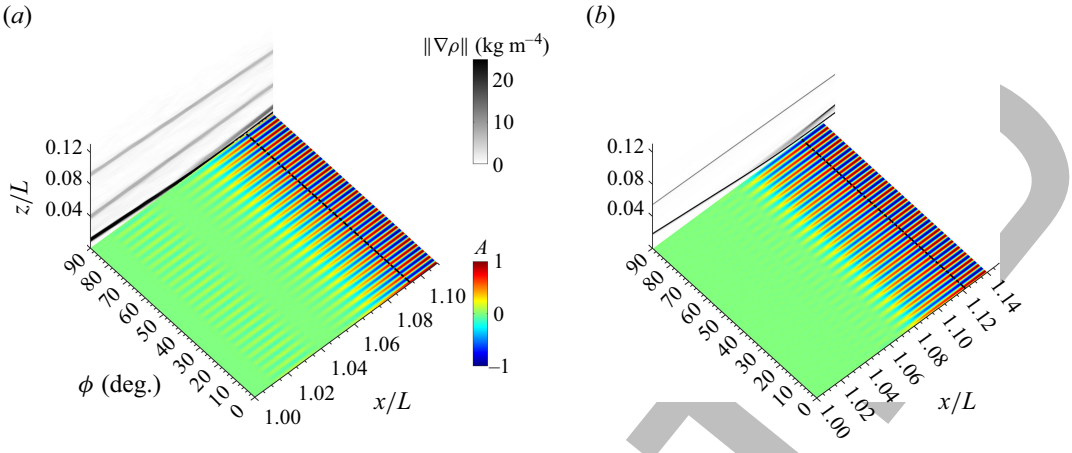


Figure 32. Value of $||\nabla\rho||$ and surface-heating mode shape. Here, $m = 100$, $Re_\infty = 5.8 \times 10^6$ m^{-1} and $r_n = 0.99$ mm. (*a*) Experiment, (*b*) DNS (saturated).

evidence that global instability of the separation bubble exists and plays a key role in the formation of the reattachment streaks for this flow.

As shown in figure 30, the $m = 100$ harmonic also exhibits considerable energy content in the POD energy spectra for both the experiment and saturated regime of DNS. Figure 32 displays its azimuthally reconstructed POD mode shape. The harmonic exhibits two dissimilarities from the fundamental: the harmonic does not have a neutral line and sign change at reattachment, and its oscillations have low amplitude until much closer to reattachment.

To determine whether the global instability of the separation bubble dominates at higher free-stream unit Reynolds numbers and nose radii, Fourier decomposition coupled with POD was performed on the thermographs for various Re_∞. Figure 33 presents the energy spectrum as a function of wavenumber for $r_n = 0.99$ mm. As Re_∞ increases, the most energetic azimuthal wavenumber also increases, consistent with GSA and DNS predictions. At low Re_∞ (figure 33*a*), energy is concentrated in a few wavenumbers, whereas at high Re_∞ (figure 33*b*), it is distributed across many more. Convective mechanisms excite a broad range of wavenumbers (Dwivedi *et al.* 2019; Lugrin *et al.* 2022*b*; Davami *et al.* 2025*d*). At higher Re_∞, turbulence near reattachment and nonlinear interactions across frequencies and scales broaden the energetic wavenumber distribution.

Figure 34 compares dominant azimuthal wavenumbers from experiment and the linear growth regime of DNS with the wavenumbers with the largest growth rate computed from GSA for varying Re_∞ and nose radii. For both experiments and GSA, as Re_∞ increases, the dominant azimuthal wavenumber increases. Furthermore, at a given Re_∞, a blunt nose yields a smaller dominant wavenumber than the sharper noses. This is likely due to a blunter nose resulting in a more stable flow on the conical forebody, leading to a larger separation bubble, and delayed transition in the reattachment region. This explains why past studies of flare-induced SWBLIs with relatively sharp noses have reported striations that are challenging to detect: the earlier onset of turbulence and higher-wavenumber striations necessitate high-spatial-resolution measurements.

The dominant wavenumbers from experiment agree excellently with those from GSA – no more than 7 % different, which is within the measurement precision – except for sharper noses at $Re_\infty > 10.0 \times 10^6$ m^{-1}. There are two reasons that the concordance

https://doi.org/10.1017/jfm.2025.10905

RETRACTED

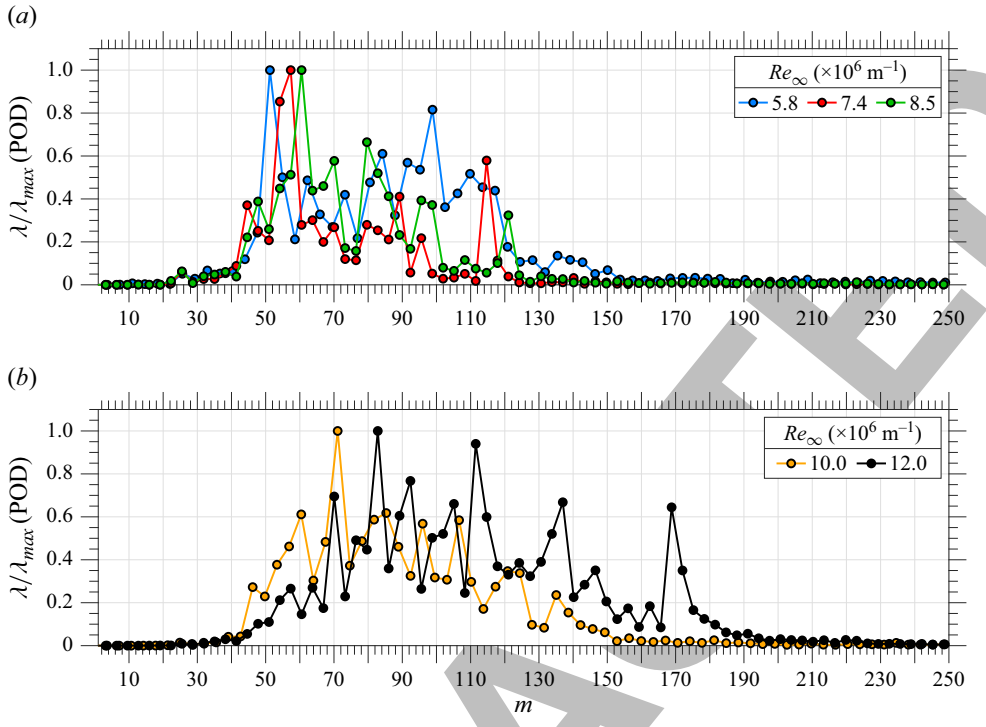


Figure 33. Normalised spectral-POD wavenumber energy from experiment ($r_n = 0.99$ mm); (*a*) $Re_\infty = 7.6 \times 10^6$ to 8.5×10^6 m^{-1}, (*b*) $Re_\infty = 10.0 \times 10^6$ to 12.0×10^6 m^{-1}.

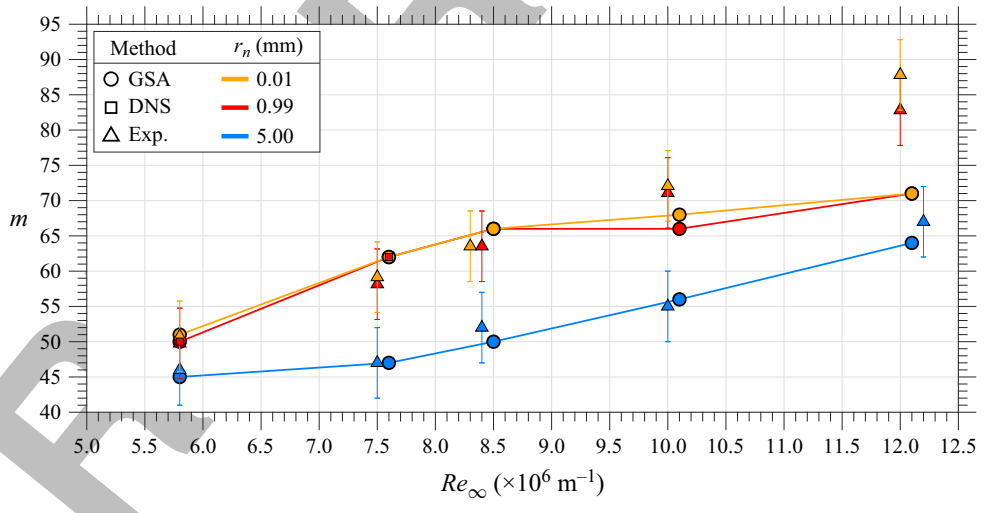


Figure 34. Dominant azimuthal wavenumbers from GSA, DNSs and experiment.

between GSA and experiment would be worse for this case. First, recalling figure 9, GSA predicted rather uniform growth rates for wavenumbers near the maximum growth for sharp noses at $Re_\infty = 12.1 \times 10^6$ m^{-1}. Growth rates differed by only 2.5 % for wavenumbers from $m = 60$ to 85, a wide range of wavenumbers with growth rates very

https://doi.org/10.1017/jfm.2025.10905

close to the maximum. Second, although all Re_∞ examined in this study resulted in a separation bubble, at higher Re_∞ and for sharper nose radii, the separation bubble becomes significantly smaller, indicating the transition front is only slightly downstream of the cone–flare junction. Under these conditions, the flow enters a nonlinear regime where linear GSA is no longer valid. However, the excellent agreement among GSA, DNS, and experiment for the lower Re_∞ cases is yet more evidence strongly indicating that the global instability within the separation bubble causes the heating streaks at reattachment for this configuration.

7.2. *Off-wall dynamics*

The dynamics of the separation bubble was analysed globally by applying spectral-POD (SPOD) to the high-speed BOS measurements and DNS. It is a data-driven method that extracts coherent structures from flow field measurements by considering both spatial and temporal modes, unlike traditional POD, which only analyses spatial modes (Schmidt & Shepherd 2020). Using a space–time inner product, SPOD decomposes flow snapshots into energetically optimal modes at distinct frequencies, with leading modes generally corresponding to coherent spatial structures (Towne, Schmidt & Colonius 2018).

Figure 35 presents the normalised SPOD mode energy spectrum for $r_n = 0.99$ mm and various Re_∞. The decomposition was applied to the BOS-measured density gradient, computed from 31 blocks of 128 snapshots with 50 % overlap, resolving frequencies up to 15 kHz (Nyquist limit). The spectrum reveals the distribution of energy across spatio-temporal modes, emphasising the dominant frequencies and spatial patterns that drive the dynamics of the system. As explained by Schmidt & Shepherd (2020), a significant separation between the first and second SPOD modes indicates the dominance of a particular mechanism. For this flow, the primary mechanism is unsteadiness along the shear layer and at reattachment. The first and second modes in the spectrum are separated in the frequency range of 1 to 5 kHz, with the gap widening as Re_∞ increases.

Although the stationary global unstable mode was detected both experimentally and in simulations by leveraging spatial spectral analysis of the surface heat flux, extracting it from off-wall temporal measurements is profoundly challenging, because it appears at zero frequency and is thus dominated by the mean flow and experimental noise. Oscillatory global unstable modes should be detectable experimentally; however, they are primarily centred within the separation bubble, where BOS signal levels are low. Consequently, their unsteady influence is mainly near reattachment, where density-gradient fluctuations are stronger. Note also that in the experiment, the influences of convective amplification and global instability mechanisms are difficult to isolate (Davami *et al.* 2025*d*).

Figure 36 displays the real part of the leading SPOD mode from BOS measurements and DNS, which were both observed consistently from 1 to 5 kHz, and the real part of the density-gradient perturbation associated with the leading stationary and secondary oscillatory global unstable mode identified through GSA for $Re_\infty = 5.8 \times 10^6$ m^{-1} and $r_n = 0.99$ mm. The ordinate is the normalised wall-normal coordinate, and the white line indicates the boundary-layer edge for attached flow or the shear-layer location for separated flow. This location is determined as the wall-normal height corresponding to the peak vertical density gradient, a criterion validated in Davami *et al.* (2025*c*).

The four results in figure 36 exhibit a similar spatial structure, with anti-correlated lobes at the reattachment region. The agreement in frequency and spatial structure suggests that the oscillatory global mode was detected experimentally. The stationary global mode ($f = 0$ kHz) reflects the spatial structure of the reattachment region and indicates a persistent flow pattern on which the oscillatory instabilities are superimposed. The

RETRACTED

https://doi.org/10.1017/jfm.2025.10905

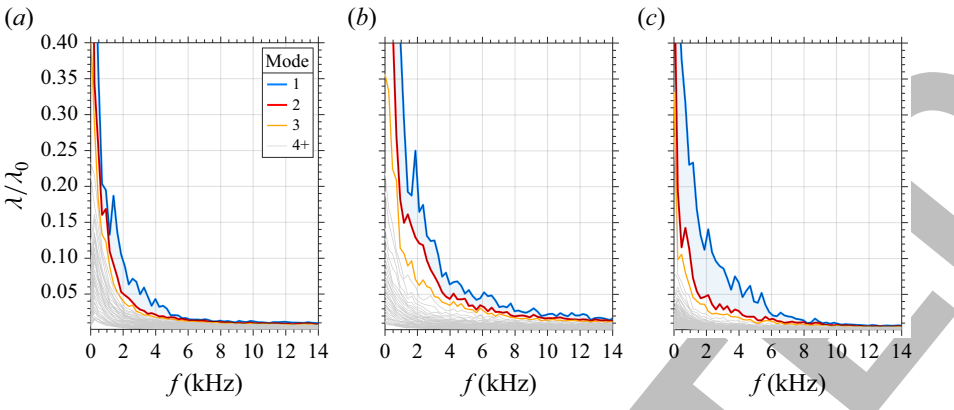


Figure 35. Normalised SPOD energy spectra of high-speed BOS measurements ($r_n = 0.99$ mm); (*a*) $Re_\infty = 5.8 \times 10^6$ m^{-1}, (*b*) $Re_\infty = 8.5 \times 10^6$ m^{-1}, (*c*) $Re_\infty = 12.0 \times 10^6$ m^{-1}.

other global oscillatory unstable modes from GSA (not shown) display nearly identical perturbation modes localised at reattachment. Note that the line-of-sight integration inherent to BOS, combined with the finite aperture and depth of field, distorts the experimentally measured mode shape.

Similar low-frequency modes – previously thought to arise from mainly convective mechanisms near reattachment – have been reported for this geometry in multiple high-speed facilities, both noisy and quiet (Davami & Juliano 2024; Benitez *et al.* 2024*b*; Davami *et al.* 2025*a*,*d*). Additionally, for this geometry and flow conditions, off-wall convective mechanisms at higher frequencies (25–40 kHz), including shear-layer instabilities and shock-layer waves, have been measured in the separation region and at reattachment (Benitez *et al.* 2023; Davami *et al.* 2024*a*, 2024*b*; Davami *et al.* 2025*a*,*c*,*d*), along with significantly higher-frequency second-mode waves (200–290 kHz) (Butler & Laurence 2021, 2022; Sousa & Laurence 2025).

7.3. *Comparison of surface and off-wall dynamics*

Figure 37 presents unsteady, simultaneously measured, surface and off-wall results for $Re_\infty = 5.8 \times 10^6$ to 12.0×10^6 m^{-1} and $r_n = 0.99$ mm. The centre contour shows the azimuthally reconstructed POD mode shape of the most energetic azimuthal wavenumber (POD of $\mathcal{F}(St')$). Above it, the high-resolution BOS-measured magnitude of the density gradient ($||\nabla\rho||$) is shown for off-wall context of the mean flow, while the bottom contour displays the leading SPOD mode shape from high-speed BOS measurements of the density gradient (SPOD $\nabla\rho$). Included for reference in the off-wall mode shapes are the shear-layer edge (grey dashed line) and the separation shock (grey solid line).

The experimentally measured streamwise heat-flux perturbations in figure 37 extend from within the recirculation bubble and amplify downstream of reattachment. Furthermore, near reattachment, they exhibit a sign change, and the neutral line shifts upstream with reattachment as Re_∞ increases. At $Re_\infty = 7.6 \times 10^6$ m^{-1}, the azimuthally reconstructed real part of the streamwise heat-flux perturbation of the leading stationary disturbance computed by GSA, resembles that observed at $Re_\infty = 5.8 \times 10^6$ m^{-1} (figure 31*b*). However, the first band of elevated amplitude, which is induced by the global instability, spans a much shorter streamwise distance – approximately one-third the length. The low heat-flux magnitude upstream of reattachment, combined with the diminished

RETRACTED

https://doi.org/10.1017/jfm.2025.10905

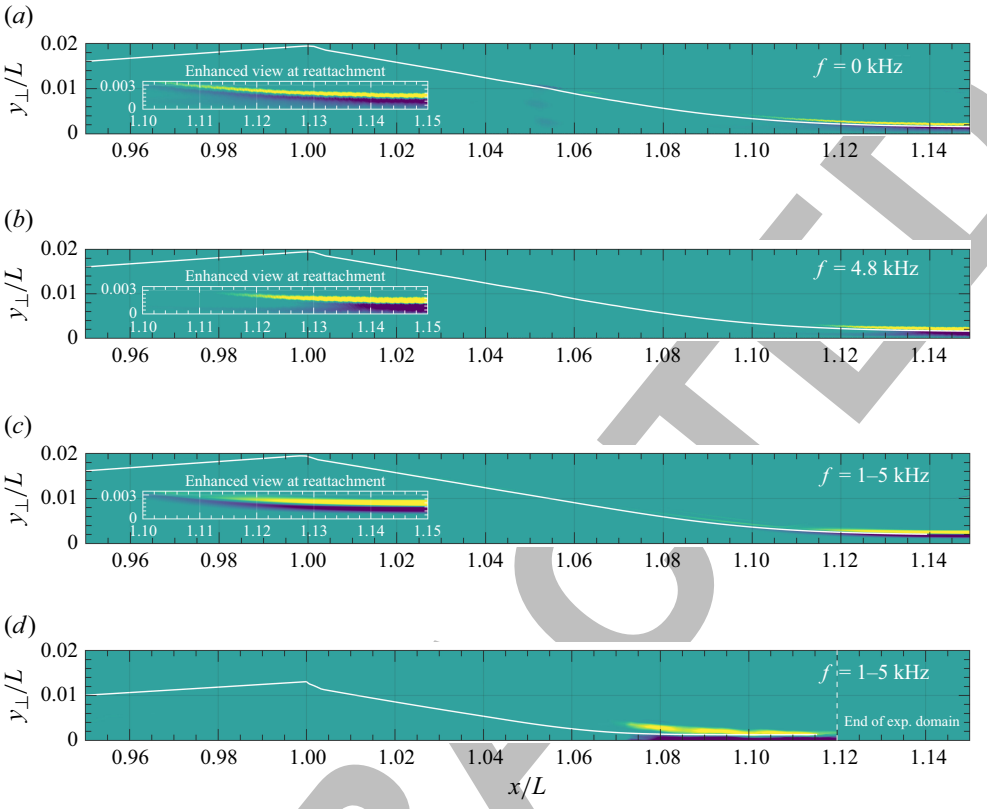


Figure 36. Real part of the leading SPOD mode from experiment and DNS, and the stationary leading and secondary oscillatory global unstable modes from GSA ($Re_\infty = 5.8 \times 10^6$ m^{-1} and $r_n = 0.99$ mm); (*a*) GSA: $m = 50$ and $f = 0$ kHz, (*b*) GSA: $m = 53$ and $f = 4.8$ kHz, (*c*) DNS: $f = 1$–5 kHz (SPOD), (*d*) experiment: $f = 1$–5 kHz (SPOD).

extent of this band, may explain why POD for the higher Re_∞ cases does not capture the sign change in the heat-flux perturbations associated with the global instability in that region.

Like for $Re_\infty = 5.8 \times 10^6$ m^{-1}, at $Re_\infty = 7.6 \times 10^6$ and 8.5×10^6 m^{-1}, the harmonics of the dominant surface-heating wavenumbers also contain elevated energy in the POD energy spectrum. Also like at lower Re_∞ (figure 32*a*), other higher harmonics amplify near the end of the flare. At $Re_\infty = 10.0 \times 10^6$ and 12.0×10^6 m^{-1}, the streaks experience less amplification because transition to turbulence occurs farther upstream. At the highest Re_∞, the dominant wavenumber has high amplitude only near reattachment (figure 37*e*), while its harmonic and others with significant energy amplify farther downstream (not shown).

The SPOD modes of the off-wall density gradient (i.e. SPOD($\nabla\rho$), lower contour) exhibit an alternating fluctuation pair straddling the shear layer and centred near reattachment. The frequency range over which these modes appear broadens with increasing Re_∞, reflecting elevated unsteadiness along the shear layer and around the reattachment region as the flow transitions. For each Re_∞, the sign changes in the off-wall oscillations correspond closely to those of the streamwise heat-flux instability modes. Since heat flux scales with density (Running *et al.* 2020; Davami *et al.* 2025*c*),

RETRACTED

https://doi.org/10.1017/jfm.2025.10905

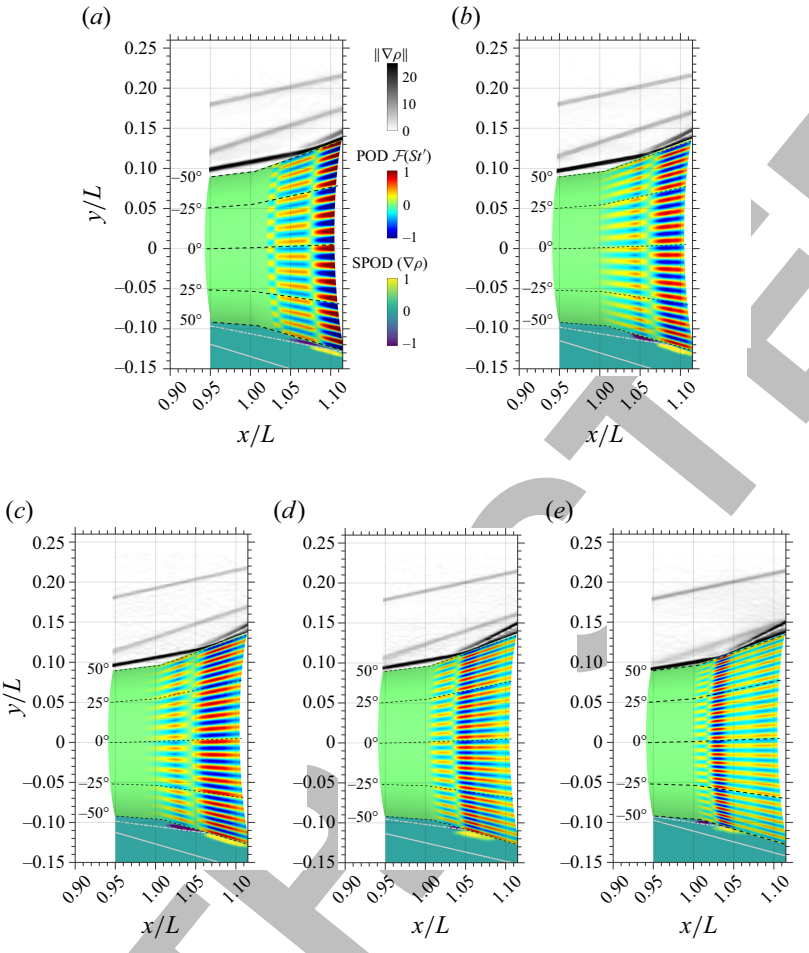


Figure 37. Simultaneous, global experimental measurements of the unsteady-flow dynamics ($r_n = 0.99$ mm): (*a*) 5.8×10^6 m^{-1}, $m = 50$ and $f_{SPOD\nabla\rho} = 1 - 5$ kHz; (*b*) 7.6×10^6 m^{-1}, $m = 58$ and $f_{SPOD\nabla\rho} = 1 - 5$ kHz; (*c*) 8.5×10^6 m^{-1}, $m = 63$ and $f_{SPOD\nabla\rho} = 0.5 - 6$ kHz; (*d*) 10.0×10^6 m^{-1}, $m = 71$ and $f_{SPOD\nabla\rho} = 0.5 - 6$ kHz; (*e*) 12.0×10^6 m^{-1}, $m = 82$ and $f_{SPOD\nabla\rho} = 0.5 - 7$ kHz.

these coupled oscillations shift upstream in tandem with the reattachment location as Re_∞ increases.

8. Concluding remarks

Computational and experimental investigations were conducted on a nominally axisymmetric, transitional separation bubble over a cone–flare in hypersonic flow. Instabilities in separation and at reattachment, induced by the SWBLI, were measured simultaneously using IR thermography and high resolution, high-speed BOS measurements. The experiments were performed in the AFOSR–Notre Dame Large Mach-6 Quiet Tunnel under conventional-noise conditions, with free-stream unit Reynolds numbers ranging from 5.8×10^6 to 12.3×10^6 m^{-1}, and at a nominally zero angle of attack. The model consisted of a 7° half-angle circular cone and a 20° half-angle flare, with three different nose radii: $r_n = 0.01$, 0.99 and 5.00 mm. Computational investigations matched the experimental geometry and flow conditions. Laminar and turbulent base

RETRACTED

https://doi.org/10.1017/jfm.2025.10905

flows were computed, with stability analysis combining PSE, HLNSE and GSA. Direct numerical simulations provided further comparison.

The mean flow was investigated first. Infrared thermography assessed flow stability and evaluated the boundary-layer state through calculation of the laminar and turbulent heating rates. Both laminar and transitional separation were observed. For an incoming laminar boundary layer, the point where the Stanton number begins to decrement correlates with off-wall measurements of flow separation. For free-stream unit Reynolds numbers below 10.0×10^6 m^{-1}, the boundary layer on the flare was transitional. The experimental peak St exceeded the time-averaged DNS predictions by more than a factor of two, which is consistent with previous SWBLI experiments indicating that heating levels in conventional noise exceed those in quiet flow. However, during the saturated growth regime of the DNS, brief, elevated spurts of heating were similar to experimental and RANS-computed results. High-resolution BOS provided quantitative off-wall density and gradient fields that closely matched computations.

By leveraging both surface and off-wall measurements, trends in separation, reattachment and transition locations were documented for varying Reynolds numbers and nose radii. For both experiment and computation, a blunter nose results in a larger separation bubble. A separation bubble was present for all Re_∞ in the experiment, with its mean length decreasing as Re_∞ increased due to the downstream shift of the separation point. This indicates a transitional interaction, where the flow is laminar before separation and becomes transitional or turbulent upon reattachment at higher Re_∞. In contrast, fully laminar base flows show increasing separation length with Re_∞ and predict larger separation regions than experiments. This difference in trends between experiment and computation has been consistently reported in both noisy and quiet-flow conditions and highlights the need for improved transitional models for flows with SWBLIs (Davami *et al.* 2025*c*, 2025*d*; Leidy *et al.* 2025).

To explain the observed differences in heating rates along the flare between experiment and simulation, additional numerical simulations were performed by imposing broadband inflow disturbances. By varying the amplitude of the inflow forcing, this study demonstrates that DNS can accurately reproduce experimental flare-heating trends, highlighting that reattachment heating on the flare is highly sensitive to inflow disturbances. Although broadband inflow forcing had negligible effect on the separation bubble length, Threadgill *et al.* (2024) and Tsakagiannis *et al.* (2025*a*) were able to contract the separation bubble length by forcing the leading convective instabilities to hasten oblique breakdown. Therefore, the inflow forcing characteristics have a profound impact on the separation bubble topology. Other factors, such as the flare length and base wake, could also impact the separation bubble. Future investigations will focus on these different factors.

To investigate whether global instability of the separation bubble drives the formation of reattachment streaks, a three-way comparison was made of the dominant azimuthal wavenumbers as computed by GSA and DNS, and measured experimentally. The dominant wavenumbers obtained from the experiment closely matched those predicted by GSA (7 % difference), except for sharper nose cases at $Re_\infty > 10.0 \times 10^6$ m^{-1}, where the difference increased to 21 %. For a sharper nose radius in the experiment, the separation bubble becomes significantly smaller, indicating the transition front is nearly upstream of the cone–flare junction. Under these conditions, the flow enters a nonlinear regime where linear GSA is no longer valid. Nonetheless, the strong agreement between the azimuthally reconstructed mode shapes and the close match of the most amplified wavenumbers from GSA and DNS confirm that global instability of the separation bubble is a dominant mechanism in the formation of the reattachment streaks. Furthermore,

RETRACTED

https://doi.org/10.1017/jfm.2025.10905

previous high-fidelity simulations showed that global unstable modes in the recirculation bubble induce streamwise sign changes in the heat-flux oscillations (Hildebrand *et al.* 2018; Sidharth & Candler 2018; Lugrin *et al.* 2022*a*). Such oscillations were indeed present in the azimuthally reconstructed dominant mode shapes obtained from surface-heating measurements. This study provides one of the first experimental confirmations of this computational prediction.

The dynamics of the separation bubble and unsteadiness at reattachment was investigated using high-speed BOS. Global spectral analysis identified the frequency range and spatial organisation of the dominant unsteady structures. The mode shapes revealed an anti-correlated pair of fluctuations concentrated along the reattachment region. The agreement in frequency and spatial structure between the experiment, DNS, and GSA modes indicates that global unstable modes can be detected experimentally. The relatively low-frequency (1–5 kHz) off-wall modes corresponded to the location of the sign change in the streamwise heat-flux instability modes for each Re_∞. Both modes shifted upstream together with reattachment as Re_∞ increased. Similar low-frequency modes have been reported previously for this geometry in multiple high-speed facilities, both noisy and quiet (Davami & Juliano 2024; Benitez *et al.* 2024*b*; Davami *et al.* 2025*a*,*d*), and attributed mainly to convective mechanisms near reattachment. However, the results reported here – from experiment, stability analysis and DNS – suggest that global modes influence, and may even dominate, over low-frequency convective mechanisms.

Supplementary movie. Supplementary movie is available at https://doi.org/10.1017/jfm.2025.10905.

Acknowledgements. The authors thank A. Leidy and Luther Jenkins for their insightful comments and valuable editing. The computational resources supporting this work were provided by the U. S. Department of Defense High Performance Computing Modernization Program and the NASA Langley Research Center K Cluster.

Funding. J.D. is supported by a University of Notre Dame Dean's Fellowship and NASA Pathways Internship. Anton Scholten is supported by the U. S. Office of Naval Research under award number N00014-23-1-2456. P.P. is supported by the Hypersonic Technology Project under the NASA Aeronautics Research Mission Directorate. N.L. and L.D. acknowledge financial support by the AFRL/DAGSI Ohio Student-Faculty Research Program and the Office of Naval Research under award number N00014-23-1-2304.

Competing interests. The authors declare none.

Data availability statement. The data that support the findings of this study are available from the corresponding author, T.J.J., upon reasonable request.

Appendix A. Grid sensitivity assessment

Additional numerical simulations are included to assess the adequacy of grid resolution. Specifically, a series of auxiliary cases were performed with a narrower spanwise domain size of $\phi = 7.2°$ (corresponding to $m = 50$), but varied grid resolution. Table 7 lists the baseline and auxiliary runs, where cases Re5.8m50Fine and Re7.6m50Fine have a higher number of grid points in the streamwise and wall-normal directions than the baseline cases.

Figures 38 and 39 show the effect of grid refinement on boundary-layer-instability growth A_w and surface heating St. Excellent agreement in the linear growth rate and saturation of A_w and the streamwise distribution of St is achieved between the baseline and grid-refined cases at both Reynolds numbers. An additional comparison between cases Re5.8 and Re5.8m50 as well as between cases Re7.6 and Re7.6m50 suggests that a narrower spanwise domain of $\phi = 7.2°$ (corresponding to $m = 50$) has a negligible

RETRACTED

https://doi.org/10.1017/jfm.2025.10905

Case	Re_∞ ($\times 10^6$ m^{-1})	ϕ (°)	$N_x \times N_\phi \times N_r$
Re5.8	5.8	90	740 × 800 × 540
Re5.8m50	5.8	7.2	740 × 64 × 540
Re5.8m50Fine	5.8	7.2	1020 × 64 × 748
Re7.6	7.6	90	740 × 800 × 540
Re7.6m50	7.6	7.2	740 × 64 × 540
Re7.6m50Fine	7.6	7.2	1020 × 64 × 748

Table 7. Summary of baseline and auxiliary DNS cases along with grid parameters.

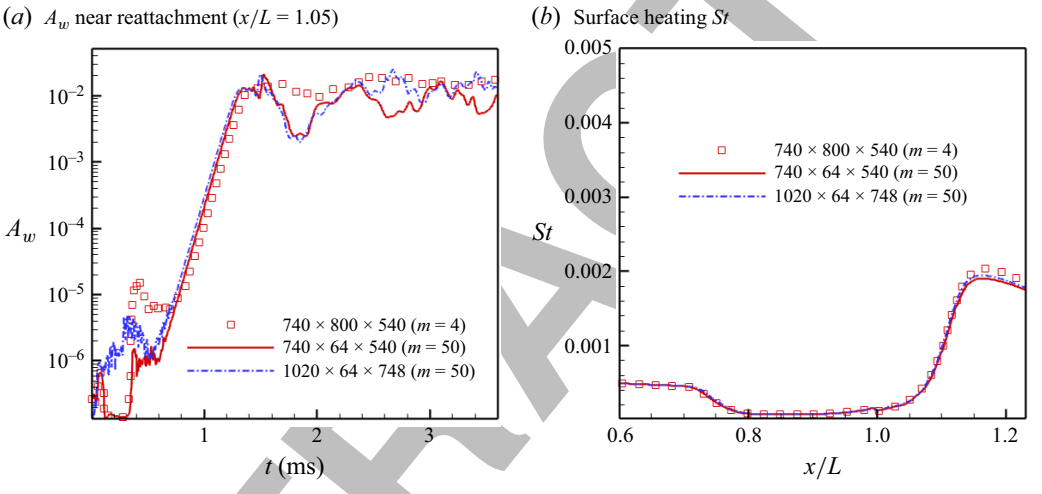


Figure 38. Grid convergence for DNS with $Re_\infty = 5.8 \times 10^6$ m^{-1} and $r_n = 0.99$ mm.

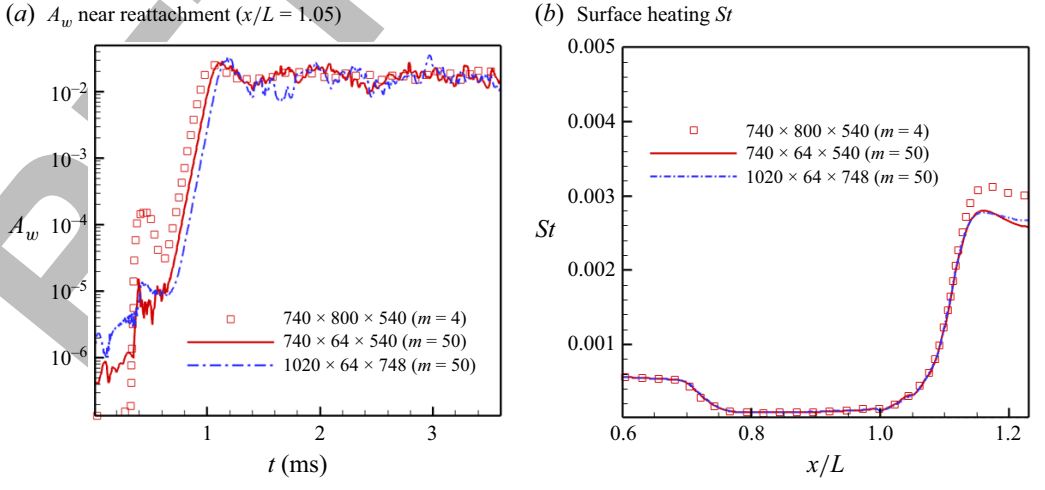


Figure 39. Grid convergence for DNS with $Re_\infty = 7.6 \times 10^6$ m^{-1} and $r_n = 0.99$ mm.

RETRACTED

https://doi.org/10.1017/jfm.2025.10905

influence on both the linear growth of global instabilities and surface heating over most of the cone–flare model except in the post-reattachment region of $x/L \geqslant 1.13$.

References

Abassi, M.A., Wang, Q. & Liu, X. 2025 Adjoint-based data assimilation in a subdomain using omnidirectional-integration-enabled pressure Dirichlet boundary conditions. *Phys. Fluids* **37** (1), 015145.

Adams, N.A. 2000 Direct simulation of the turbulent boundary layer along a compression ramp at $M = 3$ and $Re_\theta = 1685$. *J. Fluid Mech.* **420**, 47–83.

Babinsky, H. & Harvey, J.K. 2011 *Shock Wave-Boundary-Layer Interactions*, vol. 1, 1st edn., chap. 1, pp. 11–17. Cambridge University Press.

Balakumar, P., Zhao, H. & Atkins, H. 2005 Stability of hypersonic boundary layers over a compression corner. *AIAA J.* **43** (4), 760–773.

Baurle, R.A. & Edwards, J.R. 2020 Hybrid Reynolds-averaged/large-eddy simulations of hypersonic turbulent flows. *AIAA J.* **58** (6), 2567–2580.

Becker, E. 1956 Schlierenverfahren und dichtemessung in verdünnten gasen. *Z. Phys.* **145**, 566–578.

Benay, R., Chanetz, B., Mangin, B., Vandomme, L. & Perraud, J. 2006 Shock wave/transitional boundary-layer interactions in hypersonic flow. *AIAA J.* **44** (6), 1243–1254.

Benitez, E.K., Borg, M.P. & Hill, J.L. 2024*a* Nosetip bluntness effects on a cone-cylinder-flare at mach 6. *Exp. Fluids* **65** (5), 1–22.

Benitez, E.K., Borg, M.P., Hill, J.L., Davami, J. & Juliano, T.J. 2024*b* Nosetip bluntness effects on the ROTEX-T cone-flare. In *AIAA Paper* 2024-3638.

Benitez, E.K., Borg, M.P., Scholten, A., Paredes, P. & Jewell, J.S. 2023 Instability and transition onset downstream of a laminar separation bubble at Mach 6. *J. Fluid Mech.* **969**, A11.

Benitez, E.K., *et al.* 2025 Separation and transition on a cone-cylinder-flare: experimental campaigns. *AIAA J.* **63** (6), 2162–2181.

Benitez, E.K., Esquieu, S., Jewell, J.S. & Schneider, S.P. 2021 Separation bubble variation due to small angles of attack for an axisymmetric model at Mach 6. In *AIAA Paper* 2021-0245.

Berry, S.A., Horvath, T.J., Hollis, B.R., Thompson, R.A. & Hamilton II, H.H. 2001 X-33 hypersonic boundary-layer transition. *J. Spacecr. Rockets* **38** (5), 646–657.

Bibin, J., Srikanth, S., Ganesh, N. & Vinayak, K. 2016 Analysis of dimensionality effect on shock wave boundary layer interaction in laminar hypersonic flows. *Intl J. Heat Fluid Flow* **62**, 375–385.

Boyd, C.F. & Howell, A. 1994 Numerical investigation of one-dimensional heat-flux calculations. *Tech. Rep.* NSWCDD/TR-94/114. Dahlgren Division Naval Surface Warfare Center.

Brinich, P.F. 1957 Boundary-layer transition at Mach 3.12 with and without single roughness elements. *Tech. Rep.* TN 3920. NACA.

Bur, R. & Chanetz, B. 2009 Experimental study on the PRE-x vehicle focusing on the transitional shock-wave boundary-layer interaction. *Aerosp. Sci. Technol.* **13** (7), 393–401.

Butler, C.S. & Laurence, S.J. 2021 Interaction of second-mode disturbances with an incipiently separated compression-corner flow. *J. Fluid Mech.* **913**, R4.

Butler, C.S. & Laurence, S.J. 2022 Transitional hypersonic flow over slender cone/flare geometries. *J. Fluid Mech.* **949** , A37.

Caillaud, C., *et al.* 2025 Separation and transition on a cone-cylinder-flare: computational investigations. *AIAA J.* **63**, 2615–2634.

Cao, S., Hao, J. & Guo, P. 2024 Transition to turbulence in hypersonic flow over a compression ramp due to upstream forcing. *J. Fluid Mech.* **999**, A37.

Cao, S., Hao, J., Klioutchnikov, I., Olivier, H. & Wen, C.Y. 2021 Unsteady effects in a hypersonic compression ramp flow with laminar separation. *J. Fluid Mech.* **912**, A3.

de la Chevalerie, D.A., Fonteneau, A., Luca, L.D. & Cardone, G. 1997 Görtler-type vortices in hypersonic flows: the ramp problem. *Exp. Therm. Fluid Sci.* **15**, 69–81.

Chu, B.-T. 1956 On the energy transfer to small disturbances in fluid flow (Part I). *Acta Mech.* **1** (3), 215–234.

Chuvakhov, P.V. & Egorov, I.V. 2017 Numerical simulation of Görtler vortices in hypersonic compression ramp flows. *J. Appl. Mech. Tech. Phys.* **58** (2), 189–200.

Chynoweth, B.C., Edelman, J.B., Gray., K.A., McKiernan, G.R. & Schneider, S.P. 2017 Measurements in the Boeing/AFOSR Mach-6 Quiet Tunnel on hypersonic boundary-layer transition. In *AIAA Paper* 2017-3632.

Chynoweth, B.C., Lay, A. & Jewell, J.S. 2025 Boundary-layer transition on BOLT in high reynolds number Mach-6 quiet flow. *J. Spacecr. Rockets*. **62** (6), 2232–2235.

RETRACTED

https://doi.org/10.1017/jfm.2025.10905

Clemens, N.T. & Dolling, D.S. 2014 Shock wave/boundary-layer interaction dynamics in high-speed flows. *Annu. Rev. Fluid Mech.* **46**, 469–499.
Coleman, C.C. & Faruqi, F.A. 2009 On stability and control of hypersonic vehicles. *Tech. Rep.* DSTO-TR-2358. Weapons Systems Division, Defence Science and Technology Organisation, Edinburgh South Australia.
Comte, P. 1999 *Large-Eddy Simulations of Compressible Shear Flows*. In *Fluid Mechanics and its Applications Book Series*, vol. 54, chap. 1, pp. 1–12.
Currao, G.M.D., Choudhury, R., Gai, S.L., Neely, A.J. & Buttsworth, D.R. 2020 Hypersonic transitional shock-wave–boundary-layer interaction on a flat plate. *AIAA J.* **58** (2), 552–566.
Currao, G.M.D., McQuellin, L.P., Neely, A.J., Gai, S.L., O'Byrne, S., Zander, F., Buttsworth, D.R., McNamara, J.J. & Jahn, I. 2021 Hypersonic oscillating shock-wave/boundary-layer interaction on a flat plate. *AIAA J.* **59** (3), 1082–1097.
Davami, J., Chou, A., Leidy, A. & Juliano, T.J. 2023*a* Effect of roughness on BOLT-1a geometry transition in supersonic flow. In *AIAA Paper* 2023-3441.
Davami, J. & Juliano, T.J. 2024 Unsteady characteristics and enhanced determination of reattachment for hypersonic transitional shock-wave/boundary-layer interactions. In *AIAA Paper* 2024-3720.
Davami, J., Juliano, T.J., Little, N., Duan, L., Ostoich, C., Blades, E., Riley, Z.B., Benitez, E.K., Borg, M.P. & Spottswood, S.M. 2025*a* Effect of surface deformation on hypersonic transitional shock-wave/boundary-layer interactions on the ROTEX-T cone-flare. In *AIAA Paper* 2025-1307.
Davami, J., Juliano, T.J., Moreto, J.R. & Liu, X. 2025*b* Density measurements via background-oriented schlieren and parallel-ray omnidirectional integration. *Exp. Fluids* **66** (78), 1–21.
Davami, J., Juliano, T.J., Scholten, A. & Paredes, P. 2023*b* Hypersonic shock-wave/boundary-layer interactions on the ROTEX-T cone/flare. In *AIAA Paper* 2023-1436.
Davami, J., *et al.* 2024 Separation and transition on the ROTEX-T cone-flare. In *AIAA Paper* 2024-0499.
Davami, J., *et al.* 2025*c* Separation and transition on the ROTEX-T cone-flare. In *AIAA Paper* 3939-3966.
Davami, J., Leidy, A., Scholten, A., Juliano, T. & Paredes, P. 2025*d* Instability and transition on the ROTEX-T cone-flare in supersonic quiet flow. *AIAA Paper* 2025-3829.
De Tullio, N., Paredes, P., Sandham, N.D. & Theofilis, V. 2013 Laminar–turbulent transition induced by a discrete roughness element in a supersonic boundary layer. *J. Fluid Mech.* **735**, 613–646.
Duan, L., *et al.* 2018 Characterization of freestream disturbances in conventional hypersonic wind tunnels. *J. Spacecr. Rockets* **56** (2), 357–368.
Dwivedi, A., Sidharth, G.S. & Jovanović, M.R. 2022 Oblique transition in hypersonic double-wedge flow. *J. Fluid Mech.* **948**, A37.
Dwivedi, A., Sidharth, G.S., Nichols, J.W., Candler, G.V. & Jovanovic, M.R. 2019 Reattachment streaks in hypersonic compression ramp flow: an input–output analysis. *J. Fluid Mech.* **880**, 113–135.
Edney, B. 1968 Anomalous heat transfer and pressure distributions on blunt bodies at hypersonic speeds in the presence of an impinging shock. *Tech. Rep.* Report 115. FFA, Stockholm, Sweden.
Fedorov, A. 2011 Transition and stability of high-speed boundary layers. *Annu. Rev. Fluid Mech.* **43**, 79–95.
Franko, K.J. & Lele, S.K. 2013 Breakdown mechanisms and heat transfer overshoot in hypersonic zero pressure gradient boundary layers. *J. Fluid Mech.* **730**, 491–532.
Ginoux, J.J. 1965 Effect of Mach number on shock wave-boundary layer interaction. *Tech. Rep.* TN-42. Von Karman Institute.
Ginoux, J.J. 1971 Shock wave-boundary layer interaction in hypersonic flow. *Tech. Rep.* TN-71. Von Karman Institute.
Gómez, F., Le Clainche, S., Paredes, P., Hermanns, M. & Theofilis, V. 2012 Four decades of studying global linear instability: progress and challenges. *AIAA J.* **50** (12), 2731–2743.
Grasso, F. & Marini, M. 1996 Analysis of hypersonic shock-wave laminar boundary-layer interaction phenomena. *Comput. Fluids* **25** (6), 561–581.
Gray, W.D. 1967 Boundary layer transition on a 10° cone at Mach 8. *AIAA J.* **5** (5), 908–914.
Green, J.E. 1970 Interactions between shock waves and turbulent boundary layers. *Prog. Aerosp. Sci.* **11**, 235–260.
Görtler, H. 1940 Über eine dreidimensionale instabilität laminarer grenzschichten an konkaven wänden. *Gesellschaft der Wissenschaften Zu Göttingen* **2**, 1–26.
Hader, C. & Fasel, H.F. 2018 Towards simulating natural transition in hypersonic boundary layers via random inflow disturbances. *J. Fluid Mech.* **847**, R3.
Hader, C. & Fasel, H.F. 2020 Three-dimensional wave packet in a Mach 6 boundary layer on a flared cone. *J. Fluid Mech.* **885**, R3.

PEER REVIEWED

https://doi.org/10.1017/jfm.2025.10905

HAO, J., CAO, S. & WEN, C.Y. 2021 Numerical study of hypersonic compression corner flows with Görtler vortices. *AIAA J.* **59** (6), 2156–2168.
HARALICK, R.M. 1980 Digital step edges from zero crossing of second directional derivatives. *IEEE Trans. Pattern Anal. Mach. Intell.* **PAMI-2** (1), 58–68.
HILDEBRAND, N., DWIVEDI, A., NICHOLS, J.W., JOVANOVIĆ, M.R. & CANDLER, G.V. 2018 Simulation and stability analysis of oblique shock-wave/boundary-layer interactions at Mach 5.92. *Phys. Rev. Fluids* **3** (1), 1–23.
HILL, J.L., ODDO, R.A., KOMIVES, J.R., REEDER, M.F., BORG, M.P. & JEWELL, J.S. 2022 Experimental measurements of hypersonic instabilities over ogive-cylinders at mach 6. *AIAA J.* **60** (8), 4492–4508.
HOBERG, E.M. & JULIANO, T.J. 2023 Freestream characterization and condensation detection in the AFOSR–Notre Dame Large Mach-6 Quiet Tunnel. In *AIAA Paper* 2023-1458.
HOLDEN, M.S. 1972 Shock wave–turbulent boundary layer interaction in Hypersonic flow. In *10th Aerospace Sciences Meeting, San Diego, CA, USA*.
HOLDEN, M.S. 1986 A review of aerothermal problems associated with hypersonic flight. In *AIAA Paper* 1986-0267.
HORVATH, T., BERRY, S.A., HOLLIS, B., SINGER, B. & CHANG, C.-L. 2002 Boundary layer transition on slender cones in conventional and low disturbance Mach 6 wind tunnels. In *AIAA Paper* 2002-2912.
HORVATH, T.J., BERRY, S.A. & MERSKI, N.R. 2004 Hypersonic boundary/shear layer transition for blunt to slender configurations – a NASA Langley experimental perspective. *Tech. Rep.* RTO-MP-AVT-111. NATO Science and Technology Organization.
ILIFF, K.W. & SHAFER, M.E. 1993 Space shuttle hypersonic aerodynamic and aerothermodynamic flight research and the comparison to ground test results. *Tech. Rep.* NASA TM-4499. NASA Dryden Flight Research Facility.
InfraTec. 2016 *Infrared-thermographic camera ImageIR. User Manual*.
INGER, G.R. 1977 Upstream influence and skin friction in non-separated supersonic flows. *AIAA J.* **15** (8), 1150–1156.
JIANG, G.-S. & SHU, C.-W. 1996 Efficient implementation of weighted ENO schemes. *J. Comput. Phys.* **126** (1), 202–228.
JULIANO, T.J., ADAMCZAK, D. & KIMMEL, R.L. 2015 HIFiRE-5 flight test results. *J. Spacecr. Rockets* **52** (3), 650–663.
JULIANO, T.J., JEWELL, J.S. & KIMMEL, R.L. 2021 HIFiRE-5b boundary-layer transition length and turbulent overshoot. *J. Spacecr. Rockets* **58** (2), 265–283.
KENNEDY, R.E., JEWELL, J.S., PAREDES, P. & LAURENCE, S.J. 2022 Characterization of instability mechanisms on sharp and blunt slender cones at Mach 6. *J. Fluid Mech.* **936**, A39.
LAKEBRINK, M.T., BORG, M.P. & KIMMEL, R.L. 2018 HIFiRE-5b flight test results: Computational analysis. In *AIAA Paper* 2018-3808.
LAWSON, D.J. 2025 Blockage and noise characterization in the AFOSR–Notre Dame Large Mach-6 Quiet Tunnel. Master's thesis, University of Notre Dame Department of Aerospace and Mechanical Engineering.
LEE, C. & CHEN, S. 2019 Recent progress in the study of transition in the hypersonic boundary layer. *Natl Sci. Rev.* **6** (1), 155–170.
LEE, S., ZHAO, Y., LUO, J., ZOU, J., ZHANG, J., ZHENG, Y. & ZHANG, Y. 2024 A review of flow control strategies for supersonic/hypersonic fluid dynamics. *Aerosp. Res. Commun.* **2**, 1–25.
LEES, L. & LIN, C.C. 1947 Investigation of the stability of the laminar boundary layer in a compressible fluid. *Tech. Rep.* 1360. NACA Technical Note.
LEIDY, A., DAVAMI, J., JULIANO, T.J. & CHOU, A. 2024 Preliminary measurements on the BOLT geometry in the supersonic low disturbance tunnel. In *AIAA Paper* 2024-0939.
LEIDY, A., PAREDES, P., SCHOLTEN, A., JULIANO, T.J. & DAVAMI, J. 2025 Measurements on cone-flare geometries in the supersonic low disturbance tunnel. In *AIAA Paper* 2025-3828, pp. 1–24.
LI, F., CHOUDHARI, M., PAREDES, P. & SCHOLTEN, A. 2024 Nonlinear evolution of instabilities in a laminar separation bubble at hypersonic speeds. *AIAA J.* **62** (5), 1701–1711.
LIU, X. & KATZ, J. 2006 Instantaneous pressure and material acceleration measurements using a four-exposure PIV system. *Exp. Fluids* **41** (2), 227–240.
LIU, X. & MORETO, J.R. 2021 Pressure reconstruction of a planar turbulent flow field within a multiply connected domain with arbitrary boundary shapes. *Phys. Fluids* **33** (10), 101703.
LUGRIN, M., BENEDDINE, S. & GARNIER, E. 2021 Large-eddy simulation of hypersonic shock-wave/boundary-layer interaction. *J. Fluid Mech.* **918** (A22), 1–30.
LUGRIN, M., BENEDDINE, S. & GARNIER, E. 2022*a* Computational study of shock-wave/boundary-layer interaction at hypersonic speeds. *J. Comput. Phys.* **465**, 111345.

REJECTED

https://doi.org/10.1017/jfm.2025.10905

LUGRIN, M., NICOLAS, F., SEVERAC, N., TOBELI, J.P., BENEDDINE, S., GARNIER, E., ESQUIEU, S. & BUR, R. 2022*b* Transitional shockwave/boundary layer interaction experiments in the R2Ch blowdown wind tunnel. *Exp. Fluids* **63** (46), 1–19.

MACK, L.M. 1969 Boundary layer stability theory. *Tech. Rep.* Document 900-277, Rev. A. Jet Propulsion Laboratory.

MACK, L.M. 1984 Boundary-layer linear stability theory. *Tech. Rep.* No. 709. AGARD.

MAUGHMER, M.D., LONG, L.N. & PAGANO, P.J. 1992 Prediction of forces and moments for hypersonic flight vehicle control effectors. *Semi-Annual Report* NAG-849-1. Department of Aerospace Engineering, The Pennsylvania State University.

MAURIELLO, M., SHARMA, P.K., LARCHEVÊQUE, L. & SANDHAM, N. 2025 Role of nonlinearities induced by deterministic forcing in the low-frequency dynamics of transitional shock wave/boundary layer interaction. *J. Fluid Mech.* **1016**, A6.

MENTER, F.R. 1994 Two-equation eddy-viscosity turbulence models for engineering applications. *AIAA J.* **32** (8), 1598–1605.

MOLNAR, J.P., LALONDE, E.J., COMBS, C.S., LÉON, O., DONJAT, D. & GRAUER, S.J. 2024 Forward and inverse modeling of depth-of-field effects in background-oriented schlieren. *AIAA J.* **62** (11), 4316–4329.

NIESSEN, S.E.M., GROOT, K.J., HICKEL, S. & TERRAPON, V.E. 2023 Convective instabilities in a laminar shock-wave/boundary-layer interaction. *Phys. Fluids* **35** (2), 024101.

PAREDES, P. 2014 Advances in global instability computations: from incompressible to hypersonic flow. Phd dissertation, Universidad Politécnica de Madrid.

PAREDES, P., CHOUDHARI, M., LI, F., JEWELL, J., KIMMEL, R., MARINEAU, E. & GROSSIR, G. 2019*a* Nosetip bluntness effects on transition at hypersonic speeds: experimental and numerical analysis. *J. Spacecr. Rockets* **56** (2), 581–593.

PAREDES, P., CHOUDHARI, M.M. & LI, F. 2020 Mechanism for frustum transition over blunt cones at hypersonic speeds. *J. Fluid Mech.*. **894**, A22.

PAREDES, P., CHOUDHARI, M.M., LI, F., JEWELL, J.S. & KIMMEL, R.L. 2019*b* Nonmodal growth of traveling waves on blunt cones at hypersonic speeds. *AIAA J.* **57** (11), 4738–4749.

PAREDES, P., SCHOLTEN, A., CHOUDHARI, M., LI, F., BENITEZ, E.K. & JEWELL, J.S. 2022 Boundary-layer instabilities over a cone-cylinder-flare model at Mach 6. *AIAA J.* **60** (10), 6112–6124.

PRASAD, A.L.N., SARATH, K.P. & UNNIKRISHNAN, S. 2025 Influence of free stream disturbance on hypersonic boundary layer dynamics over a cone–cylinder–flare. *J. Fluid Mech.* **1016**, A55.

RAJENDRAN, L.K., ZHANG, J., BHATTACHARYA, S., BANE, S.P.M. & VLACHOS, P.P. 2019 Uncertainty quantification in density estimation from Background Oriented Schlieren (BOS) measurements. In *13th International Symposium on Particle Image Velocimetry*.

RATACZAK, J.A., RUNNING, C.L. & JULIANO, T.J. 2021 Verification of quantitative infrared thermography heat-flux measurements. *Exp. Therm. Fluid Sci.* **121**, 110274.

ROBINET, J.-C. 2007 Bifurcations in shock-wave/laminar-boundary-layer interaction: global instability approach. *J. Fluid Mech.* **579**, 85–112.

ROGHELIA, A., OLIVIER, H., EGOROV, I. & CHUVAKHOV, P. 2017 Experimental investigation of Görtler vortices in hypersonic ramp flows. *Exp. Fluids* **58**, 139.

RUNNING, C.L. 2020 Global measurements of axisymmetric hypersonic shock-wave/boundary-layer interactions. PhD thesis, University of Notre Dame.

RUNNING, C.L. & JULIANO, T.J. 2021 Global measurements of hypersonic shock-wave/boundary-layer interactions with pressure-sensitive paint. *Exp. Fluids* **62** (91), 1–18.

RUNNING, C.L., JULIANO, T.J., BORG, M.P., JEWELL, J.S. & KIMMEL, R.L. 2019 Hypersonic shock-wave boundary-layer interactions on a cone/flare. *Exp. Therm. Fluid Sci.* **109** (109911), 1–19.

RUNNING, C.L., JULIANO, T.J., BORG, M.P. & KIMMEL, R.L. 2020 Characterization of post-shock thermal striations on a cone/flare. *AIAA J.* **58** (5), 2352–2358.

RUNNING, C.L., RATACZAK, J.A., ZACCARA, M., CARDONE, G. & JULIANO, T.J. 2022 A wrap-film technique for infrared thermography heat-transfer measurements in high-speed wind tunnels. *Exp. Therm. Fluid Sci.* **135**, 110604.

SAAD, Y. 1980 Variations of Arnoldi's method for computing eigenelements of large unsymmetric matrices. *Linear Algebra Appl.* **34**, 269–295.

SAÏDI, I.B.H., WANG, S., FOURNIER, G., TENAUD, C. & ROBINET, J.-C. 2025 Modal analysis of the triadic interactions in the dynamics of a transitional shock-wave boundary-layer interaction. *J. Fluid Mech.* **1009**, A43.

SCHMIDT, B.E. & SHEPHERD, J.E. 2020 Analysis of unsteady shock motion in hypersonic inlets. *J. Spacecr. Rockets* **57** (5), 1023–1038.

REJECTED

https://doi.org/10.1017/jfm.2025.10905

SCHNEIDER, S.P. 2000 Development of a Mach-6 quiet-flow ludwieg tube for transition research. Laminar-Turbulent Transition. IUTAM Symposia. Springer, Berlin, Heidelberg.
SCHNEIDER, S.P. 2001 Effects of high-speed tunnel noise on laminar-turbulent transition. *J. Spacecr. Rockets* **38** (3), 323–333.
SCHNEIDER, S.P. 2004 Hypersonic laminar–turbulent transition on circular cones and scramjet forebodies. *Prog. Aerosp. Sci.* **40** (1–2), 1–50.
SCHOLTEN, A. 2024 Modal and nonmodal stability analysis of hypersonic flows over canonical geometries. PhD thesis, North Carolina State University.
SCHOLTEN, A., PAREDES, P., LI, F., WHITE, J., BAURLE, R. & CHOUDHARI, M.M. 2022 Automatic boundary-layer adaptation of structured grids in VULCAN-CFD. In *ICCFD11 Paper* 2022-1304.
SIDHARTH, G.S. & CANDLER, G.V. 2018 Global linear stability analysis of hypersonic boundary layers. *Phys. Rev. Fluids* **3** (7), 073401.
SIMEONIDES, G.A. 2008 Laminar-turbulent transition correlation in supersonic/Hypersonic flow – attached versus separated flow. In *26th International Congress of the Aeronautical Sciences*.
SIPP, D. & LEBEDEV, A. 2010 Global stability of base and mean flows. *J. Fluid Mech.* **645**, 333–367.
SOMBAERT, L., *et al.* 2025*a* Ground tests on BOLT at Mach 7: cross-facility comparison and stability analysis. *AIAA J.* **63** (2), 2615–2634.
SOMBAERT, L., NICOLAS, F., LUGRIN, M., SÉVÉRAC, N., ESQUIEU, S. & BUR, R. 2025*b* Hypersonic boundary-layer transition on the BOLT forebody in the R2Ch facility. *Exp. Fluids* **66**, 127.
SONG, Z. & HAO, J. 2023 Global instability of the interaction between an oblique shock and a laminar boundary layer. *Phys. Fluids* **35**, 084121.
SOUSA, C. & LAURENCE, S. 2025 Super-temporal global reconstruction of convective disturbances from images of two-dimensional flows. *Exp. Fluids* **66** (5), 1–20.
STANFIELD, S.A., KIMMEL, R.L. & ADAMCZAK, D. 2015 HIFiRE-1 flight data: turbulent boundary layer transition. *J. Spacecr. Rockets* **52** (3), 664–675.
SUN, X., YU, C., LI, X. & ZHANG, C. 2025 Mechanisms of hypersonic shock wave and turbulent boundary layer interaction on a cone/flare. *Phys. Fluids* **37** (2), 025134.
SUTHERLAND, W. 1893 The viscosity of gases and molecular force. *Lond. Edin. Dublin Phil. Mag. J. Sci.* **36** (223), 507–531.
THEOFILIS, V., HEIN, S. & DALLMANN, U. 2000 On the origins of unsteadiness and three-dimensionality in a laminar separation bubble. *Phil. Trans. R. Soc. Lond. A* **358**, 3229–3246.
THIELICKE, W. & SONNTAG, R. 2017 Particle image velocimetry for MATLAB: accuracy and enhanced algorithms in PIVlab. *J. Open Res. Softw.* **9** (1), 12.
THOMPSON, K.W. 1987 Time dependent boundary conditions for hyperbolic systems. *J. Comput. Phys.* **68** (1), 1–24.
THREADGILL, J.A.S., HADER, C., SINGH, A., TSAKAGIANNIS, V., FASEL, H.F., LITTLE, J.C., LUGRIN, M., BUR, R., CHIAPPARINO, G. & STEMMER, C. 2024 Scaling and transition effects on hollow-cylinder/flare shock/boundary-layer interactions in wind tunnel environments. *AIAA J.* **63** (4), 1228–1242.
THREADGILL, J.A.S., LITTLE, J.C. & WERNZ, S.H. 2021 Transitional shock boundary layer interactions on a compression ramp at Mach 4. *AIAA J.* **59** (12), 4824–4852.
TOWNE, A., SCHMIDT, O.T. & COLONIUS, T. 2018 Spectral proper orthogonal decomposition and its relationship to dynamic mode decomposition and resolvent analysis. *J. Fluid Mech.* **847**, 821–867.
TSAKAGIANNIS, V., HADER, C. & FASEL, H. 2025*a* Controlled transition simulations on an axisymmetric 8° compression ramp at Mach 5. In *AIAA* 2025-3605.
TSAKAGIANNIS, V., HADER, C. & FASEL, H. 2025b Numerical investigations of the linear stability regime for a separation bubble on an axisymmetric compression ramp at Mach 5. In *AIAA Paper* 2025-0077.
VENKATAKRISHNAN, L. & MEIER, G.E.A. 2004 Density measurements using the background oriented schlieren technique. *Exp. Fluids* **37** (3), 237–247.
WATTS, J.D. 1968 Flight experience with shock impingement and interference heating on the X-15-2 research airplane. *Tech. Rep.* NASA TM X-1669. NASA Flight Research Center.
WEIHS, H., LONGO, J. & TURNER, J. 2008 The sharp edge flight experiment SHEFEX II, a mission overview and status. In *AIAA Paper* 2008-2542.
WHEATON, B.M., BERRIDGE, D.C., WOLF, T.D., ARAYA, D.B., STEVENS, R.T., MCGRATH, B.E., KEMP, B.L. & ADAMCZAK, D.W. 2021 Final design of the Boundary Layer Transition (BOLT) flight experiment. *J. Spacecr. Rockets* **58** (1), 6–17.
WILLEMS, S., KLINGENBERG, F., HARGARTEN, D.A., GUELHAN, A., PLUMMER, A., THREADGILL, J.A. & LITTLE, J.C. 2024 Shock wave boundary layer interaction on the STORT flight experiment. In *AIAA* 2024-2384.
WILLIAMSON, J.H. 1980 Low-storage Runge–Kutta schemes. *J. Comput. Phys.* **35** (1), 48–56.

RETRACTED

https://doi.org/10.1017/jfm.2025.10905

XU, G., CHEN, J. & LIU, X. 2024 Görtler vortices in hypersonic boundary layers over concave surfaces. *Phys. Rev. Fluids* **9** (3), 033901.

YANG, H., LIANG, H., GUO, S., TANG, M., ZHANG, C., WU, Y. & LI, Y. 2022 Research progress of hypersonic boundary layer transition control experiments. *Adv. Aerodyn.* **4**, 18.

ZACCARA, M., EDELMAN, J.B. & CARDONE, G. 2020 A general procedure for infrared thermography heat transfer measurements in hypersonic wind tunnels. *Intl J. Heat Mass Transfer* **163**, 120419.

RETRACTED

https://doi.org/10.1017/jfm.2025.10905